BABEȘ-BOLYAI UNIVERSITY
FACULTY OF PHYSICS

OPTIMIZATION OF PHYSICO-CHEMICAL PARAMETERS OF GOLD EPITAXIAL FILMS AND BIOMOLECULAR SYSTEMS FOR IMPROVING LIFE QUALITY

Doctoral Thesis Summary

By
Alia UNGUREAN

Scientific supervisor
Prof. Dr. Leontin DAVID

CLUJ-NAPOCA
2014

BABEȘ-BOLYAI UNIVERSITY

FACULTY OF PHYSICS

Optimization of physico-chemical parameters of gold epitaxial films and biomolecular systems for improving life quality

Scientific supervisor

Prof. Dr. Leontin David

PhD student

Alia Ungurean

CLUJ-NAPOCA

2014

Contents

INTRODUCTION **2**

Deposition of gold thin films using molecular beam epitaxy technique **4**

Experimental details 4

The influence of substrate temperature on the structural and morphological properties of Au/Si(111) films 5

The influence of deposition rate on the structural and morphological properties of Au/Si(111) films 9

Theoretical and spectroscopic studies of antibiotics 12

Trimethoprim 12

Sulfamethoxazole 23

Characterization and discrimination of Gram - positive bacteria using Raman and SERS spectroscopies **33**

Experimental section 34

Raman spectra of *L. casei* and *L. monocytogenes* 37

SERS spectra of *L. casei* and *L. monocytogenes* 38

Principal component analysis of *L. casei* and *L. monocytogenes* 40

GENERAL CONCLUSIONS **44**

References 46

List of publications 49

Keywords: *MBE, STM, Raman, SERS, thin gold films, antibiotics, bacteria.*

INTRODUCTION

There is a continuous changing in our lives and in our expectations. As the informational technologies rapidly emerge, we are constantly trying to adapt to a newer and a faster way of living. In the same time, we are searching for newer, faster, more powerful and environmental friendly instruments and methods that can improve our life quality. Among these, the vibrational spectroscopy methods have attracted a considerably interest in multiple research areas, as medicine, pharmaceutical industry, and even food assurance, due to their multiple advantages over the classical methods.

This thesis was thought to be a first step in the building and the development of miniaturized sensors with high sensitivity and specificity, with applications in improving life quality. Reproducibility is a key element for a successful development of devices with sensing properties. To obtain reproducible results, the experimental procedures, methods and parameters need to be optimized. The aim of the experimental part of this thesis was to optimize the physico-chemical parameters of nanometer gold thin films, and of some biomolecular systems with possible applications in the quality life improvement.

The first step was to deposit atomically flat metallic films, which could be further used as appropriate substrates for sensor and biosensor fabrication. Two experimental parameters were varied and the structural and morphological properties of the grown films were determined using X-ray diffraction method and scanning tunneling microscopy technique.

Secondly, two well-known antibiotics (trimethoprim and sulfamethoxazole) were investigated by means of different vibrational spectroscopic methods: FTIR, FT-Raman and surface-enhanced Raman scattering (SERS) spectroscopy, as well as density functional theory (DFT) calculations. The interaction of trimethoprim with the silver surface through the pyrimidine ring, in a perpendicular orientation, was simulated by using two theoretical models. The results showed that the profile of the SERS experimental spectrum is well reproduced only by combining the two models. Sulfamethoxazole was the second characterized antibiotic by means of FTIR/ATR, FT-Raman and SERS spectroscopic techniques. For a reliable assignment of the vibrational modes of the molecule, DFT calculations were used in combination with the experimental methods. Particular emphasis was put on the adsorption geometry of the molecule to the silver

colloidal nanoparticles surface. The geometry of the molecule in the vicinity of the silver surface was quantitative determined by calculations performed on the sulfamethoxazole molecule adsorbed on a slab constructed model that simulated the Ag(111) surface.

The last goal of this thesis was to use Raman and SERS spectroscopic methods to characterize two types of Gram-positive bacteria and, based on the spectroscopic results, to discriminate them based on the Principal Component Analysis statistical technique. The studied bacteria were *Lactobacillus casei* and *Listeria monocytogenes*. The two bacterial species have very similar, almost identical Raman spectra, and their discrimination was possible only by applying multivariate statistical methods on the obtained spectra. In case of the SERS characterization, two sample preparation methods were tested and compared. Special attention was given to the spectral differences between the two types of bacteria, the common bands and the active SERS sites, depending on the sample preparation protocols. Based on their SERS spectra, the two types of Gram-positive bacteria were fairly discriminated, and the discriminating components were identified.

Deposition of gold thin films using molecular beam epitaxy technique

Gold (Au) is a well known metal with a large domain of possible applications, due to its properties. Its chemical inertness, the low processing temperature and the electrical conductivity are the main advantages that make Au one of most widely used materials in microelectromechanical systems, like MEMS and NEMS [1]. The unusual optical properties of ultrathin (less than 10 nm) Au films evaporated on transparent substrates such as mica or quartz make them excellent substrates for optical sensors [2]. The majorities of these sensors are based on the chemical affinity of various molecules towards the Au surface and have the property of self – assembling.

The interest in optimizing the deposition parameters to obtain atomically flat Au films, the influence of the post annealing treatment on the deposited films and the surface properties of the films are still hot topics. A substrate of interest for Au deposition is silicon (Si). Like carbon and germanium, Si crystallizes into a diamond cubic crystal structure, with covalently bonded atoms and a lattice spacing of 0.5431 nm, at room temperature. The unit cell contains 8 atoms, and the atoms follow a face centered cubic (fcc) Bravais lattice. In each fcc lattice point there are 2 atoms (motif): one in the lattice point and the second displaced by ¼ of the unit cell length towards the (111) direction.

Experimental details

The Au thin films were deposited on Si(111) 7×7 reconstructed wafers using a UHV Lab-10 MBE system coupled to a variable temperature VT - SPM system, both from Omicron GmbH, Germany and installed into a Clean Room of Class 100000, a facility inside the Department of Molecular and Biomolecular Physics, INCDTIM Cluj - Napoca.

P-type Si(111) chips with dimensions 3 mm × 13 mm and thickness of 0.5 mm were bought from the Institute of Electronic Materials Technology, Warsaw, Poland and used for all Au deposition experiments. Gold pellets of 99.9995 % purity were bought from Premion, Alfa, Germany. The material was put into a PBN crucible inside the MBE effusion cell and heated at a temperature of 1240 $^{\circ}$C, in case of the substrate temperature variation study, while for the modification of the deposition rate, the effusion cell was heated in the temperature range 1190 – 1300 $^{\circ}$C. For finding the appropriate substrate temperature and deposition rate, several Au films were deposited at substrate temperatures of 480 - 630 $^{\circ}$C and the deposition rates were modified in the interval 0.15 – 4.3 nm/min.

After deposition, the films were annealed for 60 minutes at the deposition temperature, then slowly cooled down to room temperature at a rate of 13 $^{\circ}C \cdot min^{-1}$.

Ex situ STM characterization was performed on the annealed Au films using a VT-SPM and the STM images were visualized using SPIP software (Scanning Probe Image Processor (SPIP) version 6.0.10 Image Metrology ApS, Lyngby, Denmark).

The 7×7 reconstruction was assessed using STM (Figure 1) and RHEED (Figure 2) measurements.

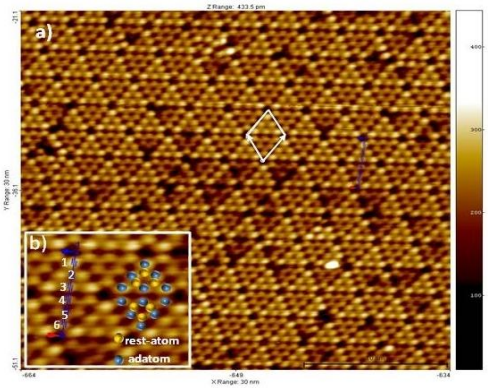

Figure 1. a) The STM image of Si(111) 7×7 reconstruction recorded by sample bias voltage of −2V and tunneling current of 0.3 nA; b) The 7×7 unit cell with schematic 12 adatoms and 6 rest atoms.

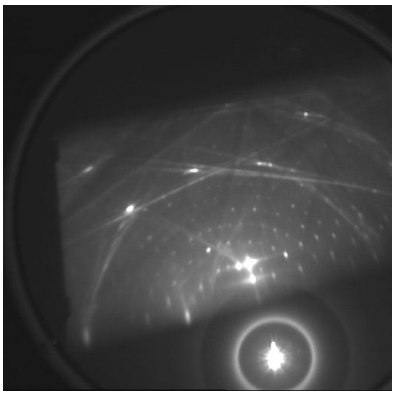

Figure 2. RHEED Si(111) 7×7 pattern obtained after well-established annealing and flashing procedure.

The influence of substrate temperature on the structural and morphological properties of Au/Si(111) films

Our first need is to develop Au thin films suitable for STM and AFM studies down to molecular resolution. It is therefore necessary to make films with low roughness, and atomic flat Au terraces. We investigated the morphology of the films prepared in the temperature range 480 - 630 $^{\circ}C$. We present 100 nm thin Au films elaborated at four different temperatures: 480 $^{\circ}C$ (film **1**), 530 $^{\circ}C$ (film **2**), 580 $^{\circ}C$ (film **3**) and 630 $^{\circ}C$ (film **4**), with a constant deposition rate of 1.6 nm/min.

- **XRD measurements**

The orientation of the thin films was studied using X-ray diffraction (XRD) in Bragg-Brentano geometry (θ-2θ). The scanning step was 0.02° with 0.8 s/step and θ–2θ range was between 10° and 90°. Figure 3 represents the normalized XRD patterns of the Au thin films deposited on Si(111) 7×7 at four different substrate temperatures.

It can be observed in the XRD diffractograms that the films deposited at lower temperatures than 580 °C contain peaks corresponding to Miller indices (111), (200), (220) and (311) which indicate that these films are not only deposited by (111) direction of the Si substrate. Film **3** with a substrate temperature of 580 °C shows two peaks corresponding to (111) direction. Peaks of Au, that could indicate other crystallographic orientation, are not identified in the XRD pattern of this thin film. This clearly suggests that the film crystallites are preferentially oriented with (111) planes parallel to the substrate [3]. With increasing temperature at 630 °C the peak corresponding to (200) planes was observed. This indicates that the film crystallites are losing their preferential orientation after (111) direction. A high substrate temperature induces defects in the films, which influence the nucleation and growth of the thin films, and finally the degradation of the crystallinity [4-9].

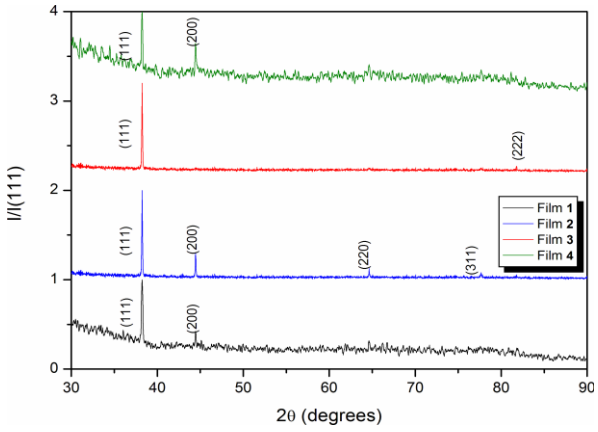

Figure 3. X-ray diffraction pattern of Au/Si(111) thin films obtained at different substrate temperatures.

Calculation of the average grain size was done using Scherrer's formula [10] and the microstrain (ε) of the grown films was estimated using the equation show in [11, 12]. For a more precise determination of the position and FWHM of the (111) peak, we performed a fitting of the experimental data with a Lorentz-type function. The average grain size for the lowest substrate temperature (480 ºC) is 40 nm. At substrate temperatures around 550 ºC the average grain size increases to a maximum value of 112.46 nm for film **3.** The microstrain behaves in an opposite manner, attending a minimum value of 0.31 at 580 ºC. The decrease of the microstrain indicates a decrease in the concentration of lattice imperfections. The evaluated structural parameters of the thin films are presented in Table 1. The smallest value of the lattice strain and the highest average grain size were attained for a substrate temperature of 580 ºC where the Au thin film presents also the best crystallinity.

Table 1
Structural parameters calculated by XRD measurements

Deposited film	Deposition temperature (°C)	B (degrees)	2θ (degrees)	D (nm)	$\varepsilon \times 10^{-3}$
1	480	0.21	38.24	40.0	0.86
2	530	0.09	38.24	92.9	0.37
3	580	0.07	38.18	112.46	0.31
4	630	0.24	38.23	35.4	0.98

- **STM characterization of the Au thin films**

Table 2 resumes the considered parameters for the obtained films. A very important parameter calculated by us, which describes the quality, and more specific, the roughness of the grown films is the root mean square (RMS) value. It should be in the range of less than 1 nm to assure that only atomic steps are present at the surface [13].

Table 2
Deposition parameters for the obtained Au films

Deposited film	Deposition temperature (°C)	Deposition rate (nm/min)	RMS (nm)
1	480	1.6	16.98
2	530		1.94
3	580		0.32
4	630		2.09

The 3D STM images used for the calculation of RMS are shown in Fig. 4, while Fig. 5 presents the morphology of the thin films at atomic scale.

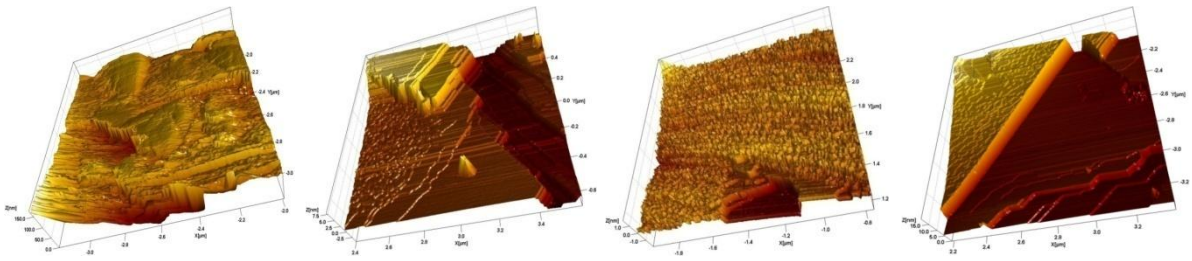

(a) **(b)** **(c)** **(d)**

Figure 4. 1.2 μm × 1.2 μm 3D STM images of the deposited thin films at different substrate temperatures. The STM images were recorded by sample bias voltage of 1.6V and tunneling current of 0.3 nA.

Our thin films show a 2D orientation, as the Fig. 4 shows. Film **1** is characterized by discontinue terraces and irregular heights, with a maximum height of ~ 150 nm. It can be seen that the grains seem to coalesce in forming a continuous surface, but is not a fully accomplished process, due to the insufficient energy given by the substrate during the deposition and annealing. In case of film **2**, the maximum height is ~ 4 nm, with wide terraces, separated mainly by monoatomic steps. An interesting observation is related to the island present in Fig. 4 (b) with the maximum height. Our thoughts go to the existing of the nucleation site. The temperature of 580 $^{\circ}$C seems appropriate for the formation of atomically smooth terraces with atomic steps measuring 3Å in height in good agreement with [14]. The film growth is layer by layer and is demonstrated in Fig, 4 (c). Finally, film **4** was grown and annealed at 630 $^{\circ}$C, having a maximum height of ~ 10 nm. The surface is made of flat terraces separated by deep holes in the range of tens of atomic layers. This is incompatible with molecular resolution STM experiments [15, 16]. Comparing the all four films, one can see the resemblance between film **2** and film **4** regarding the shape and the diameter of the grains. This phenomenon was also observed by Lussem et al. [17] during the single step process deposition of Au on mica.

The morphology of the grown thin films can be clearly observed in Fig, 5. By far, film **3** has flat atomic layers, with maximum height of ~ 0.8 nm. Film **1** is the most affected by the low deposition temperature, its surface showing rectangular shapes of different heights. The deep holes and the incomplete terraces are mostly observed in case of film **4**, due to the high deposition temperature. The maximum height is comparable with the one for film **3** (~ 0.7 nm). Finally, film **2** shows multiple flat terraces, with a maximum height of ~ 3.8 nm and incomplete terraces.

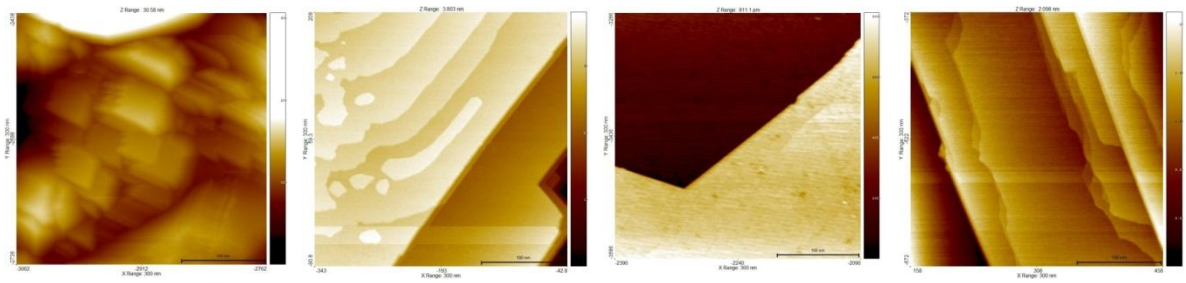

(a) **(b)** **(c)** **(d)**

Figure 5. 300 nm × 300 nm STM images of deposited thin films at different substrate temperatures. The STM images were recorded by sample bias voltage of 1.6V and tunneling current of 0.3 nA.

In conclusion, we have studied the influence of substrate temperature on the structural and morphological properties of the Au films deposited by MBE using XRD and STM characterization. XRD diffractograms show that the film deposited at 580 °C presents peaks corresponding to (111) direction and hence, the film crystallites are preferentially oriented after (111) plane parallel to the substrate. The (111) crystallographic orientation is also supported by the highest value calculated in case of the crystallites of film **3** and the lowest concentration of lattice imperfections. From STM measurements it has been found that the film deposited at 580 °C shows a good compromise between flat Au terraces which is larger than 100 nm and the lowest roughness amplitude, a necessary condition to perform STM experiments.

The influence of deposition rate on the structural and morphological properties of Au/Si(111) films

Another deposition parameter that highly influences the quality and the crystalline orientation of thin films is the deposition rate. Four deposition rates were tested: 0.15 nm/min (film **5**), 0.8 nm/min (film **6**), 1.6 nm/min (film **7**) and 4.3 nm/min (film **8**). All the films were deposited at a substrate temperature of 580 °C, previously found to be optimal [18].

- **XRD measurements**

The structural properties of the thin films were studied using XRD measurements. Figure 6 represents the normalized XRD difractograms for the films deposited at different deposition rates. It can been observed that the XRD diffractograms of the films deposited at lower deposition rate contain peaks corresponding to Miller indices (111), (200) and (220) which indicate that these films are not deposited by (111) direction of the Si substrate. The observed peak corresponding to the

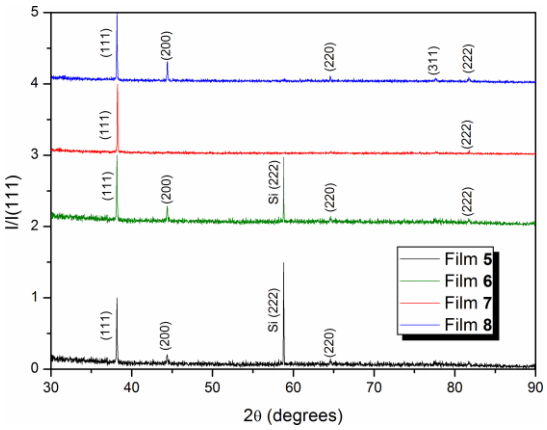

Figure 6. X-ray diffraction pattern of Au/Si(111) thin films deposited at different deposition rates.

substrate suggests that the obtained film has a low thickness. Film **7**, obtained with a deposition rate of 1.6 nm/min, shows only one peak corresponding to (111) direction. All other peaks of Au are not identified in the XRD pattern of the thin film. This fact clearly demonstrates that the film crystallites are preferentially oriented with (111) planes parallel to the substrate [46]. At a higher deposition rate of 4.3 nm/min, a polycrystalline growth was observed. During deposition, the presence of energetic particles at higher deposition rates induces defects in the films. The nucleation and the growth of the thin films are affected, leading finally to the degradation of the crystallinity [19]. The (111) peak width depends significantly on the deposition rate (see Table 3) revealing changes in the grain size.

Table 3
Structural parameters calculated by XRD measurements

Deposited film	Deposition rate (nm/min)	B (degrees)	2θ (degrees)	D (nm)	$\varepsilon \times 10^{-3}$
5	0.15	0.09	38.24	96.49	0.36
6	0.8	0.08	38.17	104.11	0.33
7	1.6	0.07	38.18	112.46	0.31
8	4.3	0.08	38.17	102.71	0.34

Using Scherrer's equation, we found out that the average grain size for the smallest deposition rate (0.15 nm/min) is 96.49 nm. By increasing the deposition rate the average grain size increase to a maximum value of 112.46 nm for the film deposition rate of 1.6 nm/min. Higher deposition rates lead to a slight reduction of the grain size, to an average of grain size of 102.71 nm. The microstrain behaves in an opposite manner attending a minimum at 1.6 nm/min. The decrease of the microstrain indicates a decrease in the concentration of lattice imperfections. The smallest value of the lattice strain and the highest average grain size were attained for 1.6 nm/min deposition rate where the Au thin film presents also the best crystallinity.

- **STM characterization of the Au thin films**

In Table 4 the considered parameters for the obtained Au films are summarized, together with the calculated RMS values.

Table 4
Deposition parameters for the obtained Au films

Deposited film	Deposition rate (nm/min)	Substrate temperature (°C)	RMS (nm)
5	0.15	580	0.19
6	0.8		1.41
7	1.6		0.02
8	4.3		0.73

The 3D STM images (Fig. 7) of the Au films were taken by applying a voltage of 1.6 V between each sample and the tungsten tip, with a detection current of 0.3 nA. All our films show a 2D orientation, independent of the deposition rate. The thickness of the films is direct proportional to the deposition rate. The surface topography of the films is very different from one film to another. While film **5**, obtained with the smallest deposition rate, have incomplete atomic terraces and only a few Au monolayers, film **8** deposited with the highest deposition rate have multiple incomplete terraces and tends to form nucleation sites on large surfaces, a phenomenon well-known in the literature [20, 21].

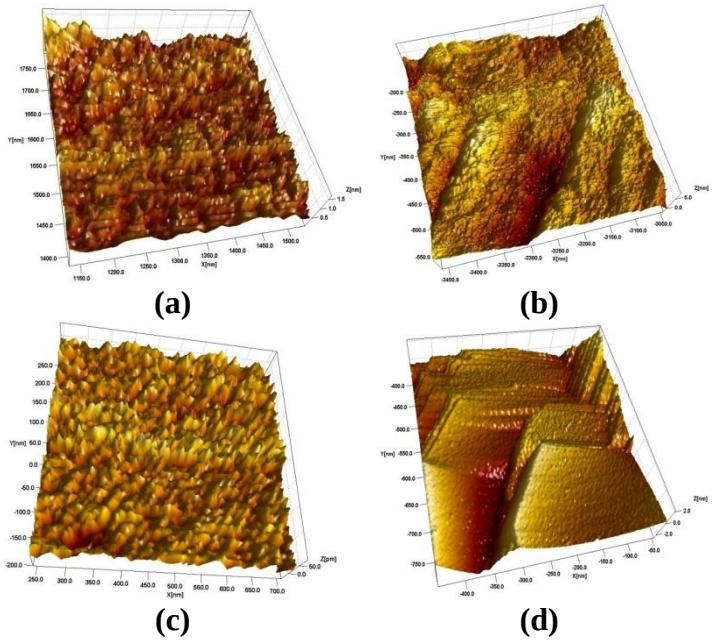

Figure 7. Representative 3D STM images of the obtained Au/Si(111) films at deposition rates of (a) 0.15 nm/min; (b) 0.8 nm/min; (c) 1.6 nm/min; (d) 4.3 nm/min.

The film deposited at 0.8 nm/min have the highest roughness, pointed out by the high RMS value. The film obtained with a deposition rate of 1.6 nm/min has atomic flat terraces and a maximum height of 0.05 nm. The growing mode for this film is layer by layer.

For Au thin films with thickness less than 100 nm a first stage of film growth consists in the nucleation of hemispherical Au clusters on the Si(111) [20]. A mixing of Au

with the interface Si atoms was also reported [22].

In conclusion, the influence of the deposition rate on the structural and morphological properties of Au films grown by MBE was thoroughly assessed using XRD and STM techniques.

XRD diffractograms show that the film deposited with an optimal rate of 1.6 nm/min has by far the most pronounced (111) crystalline orientation similar to the Si substrate. Based on the XRD measurements, we found that the grain attain the 112.46 nm maximum value for a deposition rate of 1.6 nm/min. The microstrain attains a minimum at 1.6 nm/min where the lattice imperfections seem to be the fewest.

The surface topography and the roughness of the Au/Si(111) films were evaluated by STM investigations. Flat atomic terraces thin Au films on Si(111) with very low roughness can be obtained with an optimal deposition rate of 1.6 nm/min.

The main outcome of our work is the optimal value of the deposition rate able to ensure high quality thin Au films with atomically flat terraces designed for molecular and electronic devices.

Theoretical and spectroscopic studies of antibiotics

Trimethoprim

Trimethoprim (TMP), shown in Fig. 8, is a bacteriostatic antibiotic mainly used in the prophylaxis and treatment of urinary tract infections [23, 24]. The structural investigations by vibrational spectroscopic methods (IR, Raman and SERS), as well as density functional theory (DFT) based calculations performed on trimethoprim molecule are reported in this study [25]. To the best of our knowledge, assignment of the normal vibrational modes of TMP based on IR and Raman spectroscopies coupled with quantum chemical calculations has not been done so far.

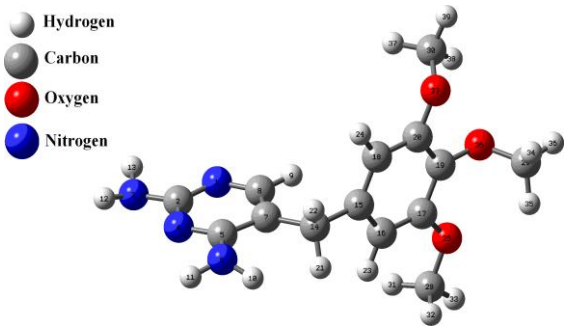

Figure 8. B3LYP/6-31G(d) optimized geometry of trimethoprim with the atom numbering scheme.

Experimental section

The FTIR spectrum of TMP powder was recorded at room temperature on a conventional Vertex 70 (Bruker, Germany) spectrometer equipped with a DTGS detector. The FT-Raman spectrum was recorded in backscattering geometry with a Bruker FRA 106/S Raman accessory equipped with a nitrogen cooled Ge detector. The 1064 nm Nd:YAG laser was used as excitation source and the laser power measured at the sample position was 350 mW. All spectra were recorded with a resolution of 2 cm^{-1} by co-adding 200 scans. The SERS spectrum was recorded using a DeltaNu Advantage spectrometer (DeltaNu, Laramie, WY) equipped with a HeNe laser emitting at 632.8 nm. The laser power was 3 mW on the sample and the spectral resolution ~10 cm^{-1}.

All chemicals used were of analytical reagent grade. The silver colloidal SERS substrate was prepared by reducing Ag^{+} with hydroxylamine [26]. The pH value of the silver colloid, measured immediately after preparation, was found to be 10.

The molecular geometry optimizations and vibrational spectra calculations were performed with the Gaussian 09 software package [27], by using density functional theory (DFT) methods with B3LYP hybrid exchange-correlation functional and the standard 6-31G(d) basis set [28, 29] for TMP molecule and the two complexes. In case of the Ag_{20} cluster, the optimization was made with B3LYP/DGDZVP combination, this level being shown to be fully adequate for optimization of silver models [30]. No symmetry restriction was applied during geometry optimization. The vibrational frequencies were computed at the optimized geometry to ensure that no imaginary frequencies were obtained, confirming that it corresponds to a true minima on the potential-energy surfaces. The assignment of the experimental bands is based on the observed frequencies and intensity patterns of the experimental spectra and confirmed by establishing a one to one correlation between the observed and theoretical calculated frequencies. The calculated Raman activities (S_i) were converted to relative Raman intensities (I_i) using equation the from [31]. The computed wavenumbers have been scaled by 0.9614 as proposed by Scott and Radom [32]. Visual inspection of modes animated by using GaussView 5.0 [33] program was also used for a proper assignment of spectra, by considering both, the band positions and intensity patterns.

The IR spectra of TMP

Experimental and calculated IR spectra of TMP in the 600-3600 cm^{-1} spectral range are shown in Fig. 9, while the assignment of the most intense bands is summarized in Table 5. In the high wavenumber range the two bands at 3468 and 3313 cm^{-1} were assigned to stretching vibrations in the $N3H_2$ amino group, the calculated bands being present at 3567 and 3451 cm^{-1}. The next region of the FTIR spectrum presents bands assigned to symmetric and asymmetric stretching vibrations in the $C28H_3$ and $C29H_3$ methyl groups and $C14H_2$ methylene group.

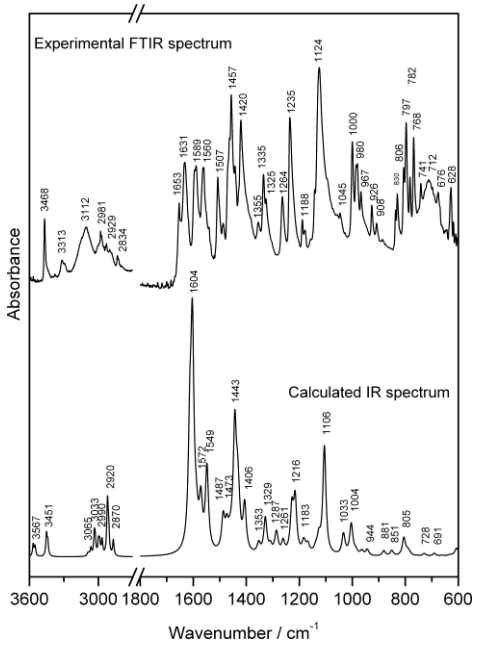

Figure 9. Experimental FTIR (top) and calculated IR (bottom) spectra of trimethoprim.

The most intense band in the IR spectrum is seen at 1124 cm^{-1} and corresponds to the stretching vibrations C-O. Other intense bands are the ones at 1457, 1420, 1235, 1000 and 797 cm^{-1}. The bands at 1457 and 1235 cm^{-1} are mainly due to bending vibrations of the amino group $N3H_2$ and the benzene ring, respectively. The band at 1457 cm^{-1} is very well reproduced by the quantum chemical calculation, both, in its position and intensity. A combination between in plane deformations in the benzene ring and bending deformations in the methyl and methylene groups give raise to the 1420 cm^{-1} band. The band located at 1000 cm^{-1} is related to a CO stretching vibrations, while the band at 797 cm^{-1} was assigned to out of plane bending deformations of the pyrimidine ring. In the experimental FTIR spectrum is also present a doublet involving $N3H_2$ bending deformation at 1631 and 1653 cm^{-1}, which can be explained on the basis of different H - bonding arrangements of the molecule in the solid state [34]. These bands correspond to the band at 1604 cm^{-1} in the calculated spectrum, the difference between the intensities being explained on the basis of the state of the molecule: solid sample (for the experimental spectrum) and the gas phase (for the DFT calculations).

Table 5

Selected experimental FTIR bands, together with calculated wavenumbers of TMP

Experimental wavenumbers (cm^{-1})	Calculated wavenumbers (cm^{-1})	Band assignment
FTIR	B3LYP/6-31G(d)	
3468	3567	$\nu_{asym}(N3H_2)$
3313	3451	$\nu_{sym}(N3H_2)$
3112	3065	$\nu(C8H)$
	3033	$\nu(C30H_3)$
2981	2990	$\nu_{asym}(C29H_3)$
2929	2967	$\nu_{asym}(C28H_3)$
2902	2920	$\nu_{sym}(C29H_3)$
2834	2870	$\nu_{sym}(C14H_2)$
1653*	1604	$\delta(N3H_2)+\nu$(ring 2)
1631	1604	$\delta(N3H_2)+\nu$(ring 2)
1589	1572	$\tau(C14H_2)+\nu$(ring 1)
1560	1549	ν(ring 2, CC, CN)+δ(H11NC)+δ(H12NC)
1507	1487	$\delta(C30H_3)+\delta(C29H_3)+\delta(C28H_3)+$ ip(ring 1)
	1473	$\delta(C29H_3)+\delta(C28H_3)$
1457	1443	$\delta(N3H_2)+\nu$(N3C2)+ip(ring 2)
1420	1406	ip(ring 1)+ $\delta(C28H_3)+\delta(C30H_3)+\tau(C14H_2)$
1355	1353	$\omega(C14H_2)+\rho(N3H_2)+\nu$(ring 2)
1325	1329	ν(ring 1)+ ν(C17O)+ ν(C19O)+ν(C20O)
	1287	$\omega(C14H_2)+\nu$(ring 1)+$\rho(N6H_2)$+ip.(ring 2)
1264	1261	ip(ring 2)+$\omega(C14H_2)+\rho(N3H_2)+\rho(N3H_2)$
1235	1216	ip(ring 1)+$\nu_{asym}(O26C_2)+\omega(C29H_3)$
1188	1183	$\omega(C30H_3)+\tau(C14H_2)$
1124	1106	$\nu_{asym}(O25C_2)+\nu_{asym}(O27C_2)$
1000	1033	ν(C28O)+ν(C30O)
967	1004	ν(C29O)
926	964	γ(ring2 CH)+$\rho(C14H_2)$
908	944	$\rho(C14H_2)+\nu_{asym}(O25C_2)+\nu_{asym}(O27C_2)$
	881	γ(ring 1 C18H)
830	851	γ(ring 1 C16H)
797	805	γ(ring 2)
712	728	γ(ring 2)+$\rho(C14H_2)$
676	691	γ(ring 1)

*doublet with 1631 cm^{-1}.

ν-stretching, δ-bending, ρ-rocking, τ-twisting, ω-wagging, γ-out of plane bending, ip.-in plane, ring1: benzene ring (C15-C16-C17-C19-C20-C18), ring2: pyrimidine (N1-C2-N4-C5-C7-C8).

The Raman spectra of TMP

The theoretical and experimental spectra of TMP are presented in Fig.10 and Table 6 summarizes the assignment of the important bands. At first sight a good correlation between the calculated and the FT-Raman bands can be observed. The differences between the theory and experiment could be a consequence of the anharmonicity and of the general tendency of the quantum chemical methods to overestimate the force constants at the exact equilibrium geometry. However, the theoretical results reproduce well the experimental data and allow the assignment of the vibrational modes.

Analyzing Fig. 10 and Table 6, one can remark that the bands given by the NH_2 symmetric and asymmetric stretchings dominate the wavenumber region 3400-3600 cm^{-1}, the only band that appears in the FT-Raman spectrum being the one at 3470 (calc. 3452 cm^{-1}) and corresponds to the symmetric stretching of $N3H_2$ amino group. In the next region of the spectrum (2800-3100 cm^{-1}) are seen the CH stretching vibrations of the methyl group, pyrimidine and benzene rings.

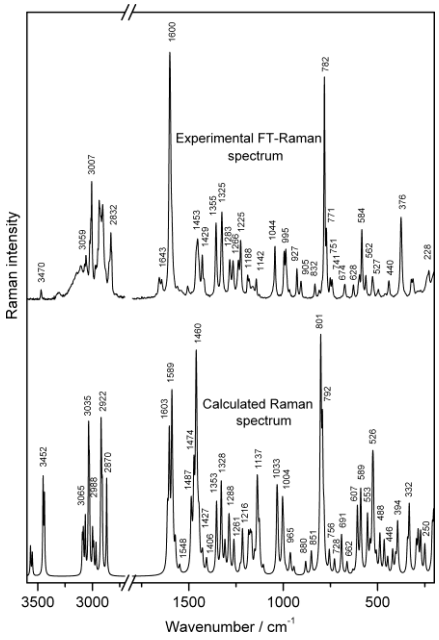

Figure 10. Experimental FT-Raman (top) and calculated Raman (bottom) spectra of trimethoprim

The stretching vibrations of benzene and pyrimidine rings combined with the twisting vibration of methylene group and the bending deformation of amino group are present in the range between 1570 and 1650 cm^{-1}. The most intense band from this region is the one at 1600 cm^{-1} (calc. 1589 cm^{-1}) and corresponds to the C-C stretchings in the benzene ring. The deformations that take place in the methyl groups are located between 1130 and 1190 cm^{-1}, while the stretching vibrations of the methoxy group are located between 990 and 1110 cm^{-1}. Other out of plane deformations are located at 927 cm^{-1} (calc. 965 cm^{-1}), corresponding to the pyrimidine-CH deformation, respectively at 832 cm^{-1} (calc. 880 cm^{-1}) corresponding to benzene-CH deformation. At lower wavenumbers in the Raman spectrum can be seen the out of plane deformation of benzene and pyrimidine ring, 751

(calc. 756 cm^{-1}) and 741 cm^{-1} (calc. 728 cm^{-1}). The second most intense band in the entire FT-Raman spectrum represents the breathing of pyrimidine ring and occurs around 782 cm^{-1} (calc. 801 cm^{-1}).

Table 6
Selected experimental SERS and FT-Raman bands, together with calculated wavenumbers of TMP

Experimental wavenumbers (cm^{-1})		Calculated wavenumbers (cm^{-1})	Band assignment
FT-Raman	SERS	B3LYP/6-31G(d)	
		3567	$\nu_{asym}(N3H_2)$
		3551	$\nu_{asym}(N6H_2)$
3470		3452	$\nu_{sym}(N3H_2)$
		3440	$\nu_{sym}(N6H_2)$
3109		3083	ν(C18H)
3059		3065	ν(C8H)
3007		3035	$\nu(C28H_3)$
		2988	$\nu_{asym}(C29H_3)$
2938		2967	$\nu_{asym}(C28H_3)$
2906		2922	$\nu_{sym}(C29H_3)$
2832		2870	$\nu_{sym}(C14H_2)$
1643	1647	1603	ν(ring 2)+$\delta(N3H_2)$
1600	1600	1589	ν(ring 1)
1561		1571	ν(ring 1)+$\tau(C14H_2)$
		1548	ν(ring 2, CC, CN)+δ(H11NC)+δ(H12NC)
1506	1503	1487	$\delta(C30H_3)$+ $\delta(C29H_3)$+$\delta(C28H_3)$ + ip(ring 1)
1453	1461	1474	$\delta(C29H_3)$+$\delta(C28H_3)$
		1460	$\rho(C29H_3)$+$\delta(C30H_3)$
1429	1406	1427	$\delta(C29H_3)$
		1406	ip(ring 1)+ $\delta(C28H_3)$+$\delta(C30H_3)$+$\tau(C14H_2)$
1355	1367	1353	$\omega(C14H_2)$+$\rho(N3H_2)$+ν(ring 2)
1325	1330	1328	ν(ring 1)+ ν(C17O)+ ν(C19O)+ν(C20O)
		1309	δ(N1C8H)+δ(C7C8H)
1283		1288	$\omega(C14H_2)$+ν(CC CH ring 1)+$\rho(N6H_2)$ + ip(ring 2)
1266		1261	ip(ring 2)+$\omega(C14H_2)$+$\rho(N3H_2)$+$\rho(N3H_2)$
1225	1227	1216	ip(ring 1)+$\nu_{asym}(O26C_2)$+$\omega(C29H_3)$
1188		1184	$\omega(C30H_3)$
1180		1173	$\rho(C28H_3)$+ $\rho(C29H_3)$
1142	1152	1137	$\rho(C30H_3)$
		1126	$\rho(N6H_2)$+ν(ring 2 CC CN)+ip(ring1 CH)
		1105	$\nu_{asym}(O25C_2)$+$\nu_{asym}(O27C_2)$

1044	1031	1033	ν(C28O)+ν(C30O)
995	993	1004	ν(C29O)
927	926	965	γ(ring2 CH)+ρ($C14H_2$)
905	903	943	ρ($C14H_2$)+ν_{asym}($O25C_2$)+ν_{asym}($O27C_2$)
832		880	γ(ring 1 C18H)
		851	γ(ring 1 C16H)
782	777	801	breathing (ring 2)
771		792	ν_{sym}(C19OC29)+ ip(ring 1) + ν(ring 2 CCC)
751	747	756	γ(ring 1)
741		728	γ(ring 2)+ρ($C14H_2$)
674	698	691	γ(ring 1)
628		662	γ(ring 1)+ρ($C14H_2$)
596	591	607	τ(ring1 C16H C18H)+ip(ring2)
584		589	ip(ring2)+ip(ring1)
562		553	Ω($N6H_2$)
527	525	526	ρ($N6H_2$)+ω($N3H_2$)
495		488	Ω($N3H_2$)
		465	ρ($N3H_2$)
440		446	ω($N3H_2$)+γ(CH ring2)
		420	Ip(ring 1)
376	370	394	δ(C17OC)+ρ($C14H_2$)
322		332	δ(C20OC30)+δ(C17OC28)+δ(C19OC29)
		285	ρ($C28H_3$)
		272	ρ(C30OC20)+ρ($C28H_3$)
228		250	ip($C5C7C14H_2$)

ν-stretching, δ-bending, ρ-rocking, τ-twisting, ω-wagging, γ-out of plane bending, ring1: benzene ring (C15-C16-C17-C19-C20-C18), ring2:pyrimidine (N1-C2-N4-C5-C7-C8), ip.-in plane

The SERS spectrum of TMP

Significant changes can be observed in band positions and relative intensities by comparing Raman and SERS spectra of trimethoprim, due to the interaction of the molecule with the silver surface (Fig. 11). Thus, the most shifted SERS bands are those observed at 698, 1406, 1031 and 1152 cm^{-1}. The SERS band at 698 cm^{-1} is blue-shifted by 24 cm^{-1} and corresponds to the bending of benzene ring. Another enhanced band that corresponds to benzene vibration is located at 1600 cm^{-1} and is assign to the stretching vibration of the ring. The band at 1406 cm^{-1} is red-shifted by 19 cm^{-1} with respect to the FT-Raman spectrum and corresponds to a bending deformation in the $C29H_3$ group. The

vibration of this group combined with another bending vibration of $C28H_3$ group is shown in the SERS spectrum by the 1461 cm^{-1} band, blue-shifted with respect to the FT-Raman spectrum. The Raman band assigned to the O27-CH_3 stretching vibration is also red-shifted from 1044 cm^{-1} in the Raman spectrum to 1031 cm^{-1} in the SERS spectrum. By far the most enhanced bands in the SERS spectrum are the ones at 777 and 1647 cm^{-1}. The first one is red-shifted by 5 cm^{-1} with respect to the FT-Raman spectrum and represents the breathing of pyrimidine ring, while the second band, blue-shifted by 4 cm^{-1}, is a combination of stretching vibration of pyrimidine and the $N3H_2$ bending deformation. That means that the part of the TMP molecule containing the pyrimidine ring and the two amino groups are located very close to the silver surface. In the SERS spectrum are also seen bands assign to the benzene ring and methoxy groups. Since their enhancement is not signifiant, we can conclude that they are far away from the silver surface. According to the SERS surface selection rules [35, 36], the normal modes, with a change in polarizability component perpendicular to the surface are enhanced. Theoretically, the interaction of TMP with the silver surface can be established through the lone electron pairs of the O and N atoms, as well as through the π electrons of the rings.

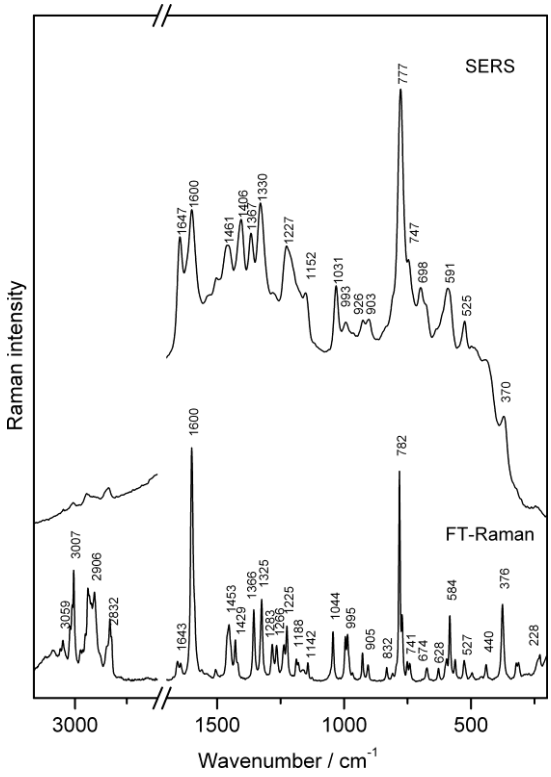

Figure 11. SERS (top) and FT-Raman (bottom) spectra of trimethoprim.

The adsorption of TMP to the silver surface is deduced based on several marker bands. Thus, taking into account the SERS result, the pyrimidine ring appears to lie perpendicular to the silver surface and the benzene ring to be oriented parallel with respect to the silver surface.

Based on the models proposed by Schatz et al. [37], we adopted a 20 – atom silver cluster and presented a detailed analysis of the enhanced Raman scattering of TMP

interacting with the cluster using DFT calculations. Two configurations were used for the simulations: a surface S-complex and a vertex V-complex (Fig. 12). The S-complex consists of an on-top binding onto one of its four faces, while the V-complex consists of binding onto one of its vertexes, which represents an ad-atom site. These two configurations were chosen due to their very different local chemical environments [37].

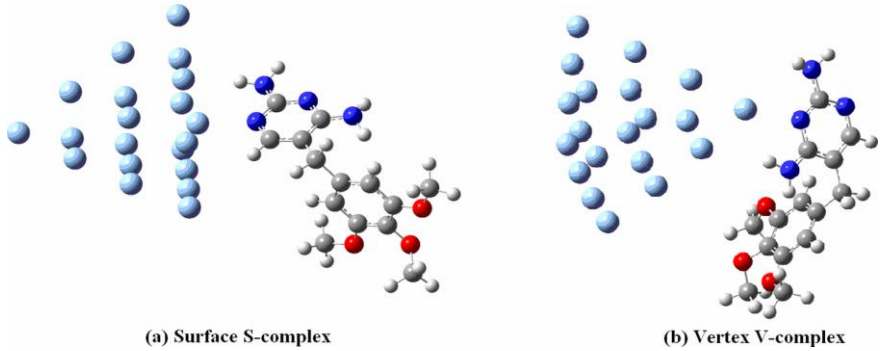

Figure 12. Optimized geometries of the two TMP-Ag20 complexes.

In case of TMP, the calculated bond distance between the N1 atom of the pyrimidine ring and the closest silver atom is 2.42 Å for the V-complex, whereas it is 2.51 Å for the S-complex. The calculated Raman spectra obtained are presented in Figures 13 (a) and (b) and are compared with the experimental SERS result.

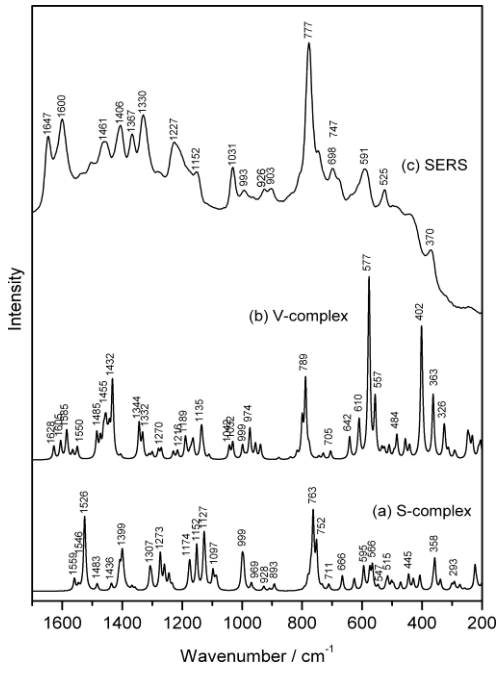

Figure 13. The calculated Raman spectra for **(a)** TMP-Ag_{20} S-complex, **(b)** TMP-Ag_{20} V-complex and **(c)** the SERS experimental spectrum.

Based on the normal band assignment, a shifting between the calculated frequencies of the V and S-complexes can be noted. Most of the V-complex bands are blue-shifted, especially at wavenumbers higher than 1040 cm^{-1}. The difference between two bands in the two models varies between 8 and 59 cm^{-1}. The biggest blue-shifting appears in case of the stretching vibration of the benzene ring. For the S-complex the band is seen at 1526 cm^{-1}, while in the V-complex spectrum it appears at 1585

cm^{-1}. The smallest blue-shifting appears for the mode that combines a rocking vibration of $C30H_3$ group and two bending vibrations (O27C30H37 and O27C30H38). This band is located at 1127 cm^{-1} and at 1135 cm^{-1}, respectively for the S and V-complex.

In case of the red-shifted bands the position of two bands in the two models varies between 4 and 55 cm^{-1}. The largest red-shifting is seen for the mode that contains a wagging and a bending deformation of the methylene group, located at 1399 cm^{-1} in the S-complex spectrum and at 1344 cm^{-1} in the V-complex spectrum. The smalest red-shifting is in case of the band at 1436 cm^{-1} in the Raman spectrum of the S-complex. This band appears at 1432 cm^{-1} in the Raman spectrum of the V-complex.

Another difference appears in the intensities of the bands and in the relative positions. The bands with high intensity in the S-complex are less intense in case of the V-complex spectrum and vice versa. The most intense bands in the V-complex are located at 577 and 402 cm^{-1}, representing wagging vibrations in the two amino groups ($N6H_2$ and $N3H_2$, respectively). Additionally, Schatz and his co-workers [37, 38] found that the intensities of the bands are sensitive to the choice of functional, so they didn't give a physical significance to this problem. In case of the S-complex the most intense bands are present at 763, 1526 and 1127 cm^{-1}.

For the V-complex, the appearance of some bands may suggest a charge transfer between TMP molecule and Ag_{20} cluster. The silver atoms involved in these vibrations are the three ones closer to the molecule, and the atoms involved from the TMP molecule from the pyrimidine ring: 3 carbon atoms (C2, C5, C7) and N4, oriented perpendicular to the V – complex. These bands are located at 363, 789 and 974 cm^{-1}. All these bands contain the stretching vibration between the nitrogen atom and the silver atom in top of the cluster. As an observation, in the range 230-210 cm^{-1} of the SERS spectrum of TMP and calculated Raman spectra of the complexes we didn't obtain bands assigned to Ag-N stretching vibration. Additionally, neither Schatz et al. [37] obtained calculated Raman bands in this region that could indicate Ag-N stretching vibrations. The SERS experimental spectrum could be seen as a combination of the two calculated Raman spectra. At high wavenumbers, the profile of the SERS spectrum is well reproduced by the V-complex (1650-1300 cm^{-1}), while in the domain of small wavenumbers is a good correlation in the position and intensity with the bands in the S-complex.

To measure the degree of association we calculated the correlation coefficients between the experimental SERS spectrum and each Raman spectrum of the two complexes (Fig. 14). The values of the correlation coefficients are 0.999 in case of the V-complex and 0.997 for the S-complex, which may suggest a better agreement between the band position in the V-complex calculated spectrum and the band position in the experimental SERS spectrum.

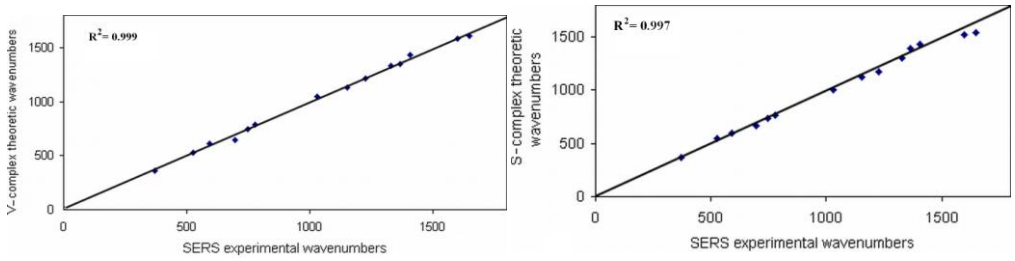

Figure 14. Plot of V-complex and S-complex theoretic wavenumbers and SERS experimental wavenumbers.

In conclusion, the recorded FTIR, FT-Raman and SERS spectra of trimethoprim were assigned based on the DFT calculated spectra. The good correlation found between the experimental and theoretical data is a clear evidence for a reliable assignment of all vibrational bands.

Based on the SERS experimental results we were able to make a qualitative determination of the molecule-silver surface interaction. It was established that the pyrimidine ring is oriented perpendicular to the silver surface, while the benzene ring is oriented parallel with respect to the silver surface.

Two models using 20-silver atoms were used to simulate the interaction between trimethoprim and the silver colloid. The calculated Raman spectra of the two possible configurations were compared with the SERS experimental results and a correlation between the band positions in all three spectra was made.

The results showed that the profile of SERS experimental spectrum is well reproduced by combining the two models.

Sulfamethoxazole

Sulfamethoxazole (4-amino-*N*-(5-methylisoxazol-3-yl)-benzenesulfonamide) (SMX), with the chemical structure shown in Fig.15 is a well known sulfonamide antibiotic used mainly in the treatment of urinary tract infections.

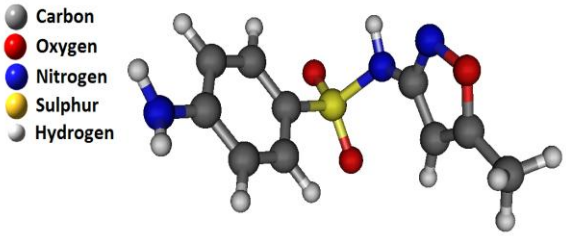

Figure 15. B3LYP/6-31G(d) optimized geometry of SMX in water.

Although sulfa drugs were of high scientific interest due to their broad spectrum of antibacterial activity [39-42], to the best of our knowledge, the adsorption of SMX on colloidal silver surface has never been investigated. Moreover, there are very few reports regarding the correlation of computational data and experimental results on this molecule [43-46]. The most recent spectroscopical data (both theoretical and experimental) of SMX have been reported by Chamundeeswari et al. [47]. **The main goal** of this work [48] was to explain the interaction of SMX with silver substrates and for this purpose we used the SERS technique, coupled to quantum chemical methods based DFT approach.

Experimental section

The FTIR/ATR spectrum of SMX powder was recorded at room temperature on a conventional 4100 Jasco FTIR spectrometer coupled with an ATR sampling device. The spectral resolution was 2 cm^{-1} and the number of scans was 30. The FT-Raman spectrum was recorded in backscattering geometry with a Bruker FRA 106/S Raman accessory equipped with nitrogen cooled Ge detector. The 1064 nm Nd:YAG laser was used as excitation source and the laser power measured at the sample position was 330 mW. The spectrum was recorded with a resolution of 2 cm^{-1} by co-adding 150 scans.

Raman aqueous and SERS spectra were recorded using a DeltaNu Advantage spectrometer (DeltaNu, Laramie, WY) equipped with a doubled frequency Nd:YAG laser emitting at 532 nm. The laser power was 40mW and the spectral resolution 8 cm^{-1}.

SMX was purchased from Sigma-Aldrich Chemical Company (>99% purity) and it was used without further purification for all experiments. At room temperature, SMX is in powder form and has a poor solubility in water at pH 7 and in organic solvents, but it is soluble in alkali hydroxides [49]. The experimental spectra were recorded at pH 10 when

the total solvation of the compound is obtained. For the Raman aqueous solution of SMX the final concentration was $7.2 \cdot 10^{-2}$ M, while for SERS sample it was found to be $3.4 \cdot 10^{-4}$ M. These concentrations were chosen due to the high resolution Raman and SERS spectra and the best signal to noise ratio.

The silver colloidal SERS substrate was prepared by Lee-Meisel method [50]. The SERS sample was obtained by mixing 500 μl Ag colloid with 25 μl of SMX solution and 15 μl NaOH solution 1M. The influence of different salts of various concentrations on the SERS signal and on the stability of the colloids [51] was studied and was found out that at least two effects may occur [52]. One of the effects refers to surface chemistry modifications, a so called "activation" with anions, that leads to a further enhancement of the signal observed from the molecule [52]. The reproducibility of our SERS spectra was confirmed by repeatedly testing the prepared SERS sample. No significant change was observed in the experimental results, which points to a stable absorption of the molecule on the silver surface.

The molecular geometry optimizations and vibrational spectra calculations were performed with the Gaussian 09 software package [27], by using density functional theory (DFT) methods with B3LYP hybrid exchange-correlation functional and the standard 6-31G(d) basis set [28, 29]. The vibrational frequencies were computed at the optimized geometry to ensure that no imaginary frequencies were obtained, confirming that it corresponds to a true minima on the potential-energy surfaces. The Raman spectrum of aqueous solution of SMX was calculated by using the Polarizable Continuum Model (PCM) [53] implemented in Gaussian 09 software, with water used as solvent. The assignment of the experimental bands is based on the observed frequencies and intensity patterns of the experimental spectra and confirmed by establishing a one to one correlation between the observed and theoretical calculated frequencies. The calculated Raman activities were converted to relative Raman intensities according to [31]. For the plot of the calculated IR and Raman spectra in gas-phase and liquid state, pure Lorentzian band shapes were used with the half width at half maximum (HWHM) of 2 cm^{-1} and 8 cm^{-1}, respectively. The computed wavenumbers have been scaled non-uniformly, using an effective scaling frequency factor (ESFF) procedure based on 9 parameters, proposed very recently by Borowski [54].

The adsorption of SMX adsorbed on a periodic slab model of the Ag(111) surface was simulated using the plane-wave based VASP software [55-57] with the GGA PBE exchange-correlation functional [58]. A plane-wave basis set with an energy cut-off of 450 eV has been employed and the electron–ion interactions were represented through the projector augmented-wave (PAW) method of Blöchl [59] as implemented in VASP [60]. The model of the Ag(111) surface was constructed based on the structure proposed by Ge et al. [61]. The length of the cell vectors a and b was set to 20.16 Å with an angle between the vectors of 92.9^{o} and c = 38.10 Å. Two layers were considered with a total of 60 Ag atoms per layer. During the calculations, the internal slab atoms were kept fixed at the bulk positions while the atoms in the top layer and molecule were allowed to relax. The Ag(111) substrate was selected since it is the most common surface used for the adsorption of molecules [62]. The size of the resulted optimized system has been reduced to 70 atoms (42 Ag atoms) for subsequent optimization with the Gaussian software, necessary for frequency calculations. For Ag atoms we used the CRENBS effective core potential and basis set [63].

Results and discussion

Sulfamethoxazole can be found in different protonation states, depending on the pH of the medium. Using the UV spectroscopy, Zhou et al. [64] obtained a pK_a value of 5.6, while through spectrophotometric titration, Boreen and coworkers [65] found that SMX can be found as three different species, with pK_a values of 1.6 and 5.7. Our calculations with the pK_a software ACD/pKa DB (Advanced Chemistry Development, Inc.) [66] have shown that SMX has the pK_avalues of 1.39 and 5.81, in good agreement with previously reported data. In our experimental studies the SMX molecule was present in the neutral form.

Regarding the DFT calculations it is important to emphasis that unlike the study of Chamundeeswari et al. [47], for theoretical calculations we used for SMX the starting geometry extracted from the crystal structure reported by Price et al. [67]. For the solid state conformer, NH group is in *cis* position to N atom in the heterocycle, while the *trans*-configuration has been utilized in ref. [47]. Using water as solvent, our B3LYP/6-31G(d) calculations reveal that *cis* conformer is about 2.9 kcal/mol (ΔG=-2.16 kcal.mol) more stable than the *trans*. This energetic difference precludes any significant contribution from the *trans* conformer to the properties of the molecule. Thus, the relative Boltzmann

populations at room temperature of the two conformers are 97.5 % and 2.5 %, for *cis* and *trans* conformers, respectively.

For calculating the solid state IR and Raman spectra of the molecule we used a model able to capture the most important hydrogen bonding interactions involving the molecules in solid state. That is, a cluster of three monomers has been extracted from the X-ray data [67] and then optimized at B3LYP/6-31G(d) level of theory. The simulated vibrational spectra were obtained after a convolution of the calculated wavenumbers with a Lorentzian line-shape as described in the computational details section. Using this procedure we obtained the simulated spectra reported in Figs. 16-18. The assignment of the experimental and calculated vibrational modes of SMX is listed in Table 7.

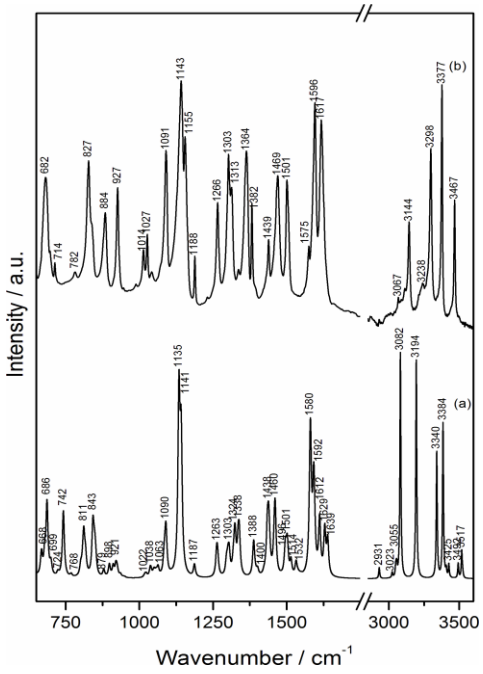

Figure 16. Theoretical IR (a) and experimental FTIR/ATR (b) spectra of SMX.

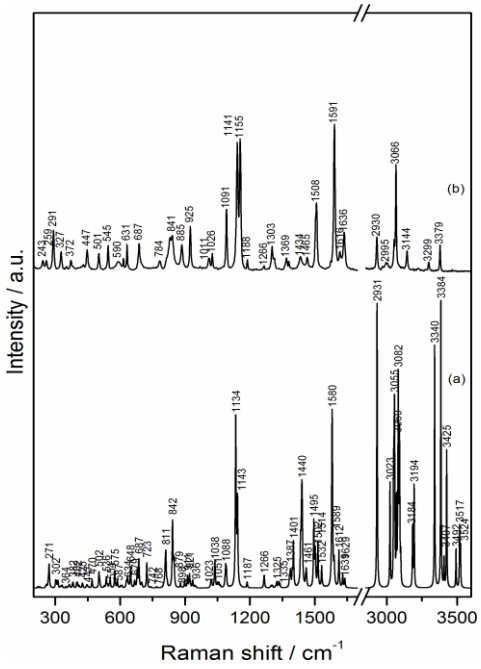

Figure 17. Theoretical Raman (a) and experimental FT-Raman (b) spectra of SMX.

Solid SMX is known to exist in three polymorphic forms [68]. By comparing our FTIR/ATR spectrum with the ones obtained in the literature [47, 68, 69], we concluded that SMX is present in form **I**. Our vibrational spectra (see Fig.16 and Fig. 17) are very similar to those reported in [45] and the assignments of normal modes are identical for most of the bands. However, according to present results, the doublet seen at 1143 and

1155 cm^{-1} (mode Q11 in Table 7) has been reassigned to the symmetric stretch of the sulphonyl group, coupled to the C-SO_2 stretching vibration. Other differences between our assignments and previously reported data [47] are observed for Q2, Q7, Q8, Q12 and Q15 modes. Here it is important mentioning that our calculations are performed on a trimer of SMX that is able to capture in a reasonable manner the most important intermolecular interactions in solid state. Thus, we are confident that these new assignments are more reliable. Actually, the doublet at 1143 and 1155 cm^{-1} is also observed in Raman and SERS spectra, red-shifted by about 30 cm^{-1}. The interaction of SMX with the silver substrate is supposed to take place via SO_2 group and this fact is supported by the new assignment of the doublet. This assignment is consistent with the findings of Lai et al. [39], although in their work the bands weren't resolved.

We would like to mention also that using the SMX trimer as model for quantum chemical calculations and the non-uniform scaling procedure [54] the XH (X=C,N) stretching vibrations are much better reproduced than in ref.[47] (see modes Q23-Q27).

A closer look at $\delta(NH_2)$ vibrations reveals that it gives rise to two bands clearly seen in the Raman spectra, at 1636 and 1616 cm^{-1}. On the other hand, only one broader band is observed in the FTIR/ATR spectrum at 1617 cm^{-1}. As seen in Table 7, the Raman band at 1636 cm^{-1} is assigned to the hydrogen bonded NH_2 group, while the 1616 cm^{-1} peak corresponds to the vibration of the free amino group.

Particular attention must be paid to the band at 1596 and 1591 cm^{-1} in FTIR/ATR and Raman spectrum, respectively. According to calculations it is a result of two vibrational modes involving mainly C=C stretchings, one of them being associated with the benzeneamide ring and the second one with the isoxazole ring. The assignment for this band is in agreement with the work of Lai et al. [39]. On the other hand, each of the two modes Q16 and Q17 is split into two bands associated with very similar vibrations in the isoxazole ring. The mode Q10 observed at 1091 cm^{-1} corresponds to a vibration almost identical to that generating the doublet Q11, however, with lower intensity.

Adsorption of SMX on the silver surface

The SERS spectrum of SMX is presented in Fig. 18, together with the experimental aqueous Raman spectrum and the theoretical Raman spectrum calculated within the PCM model, with water considered as solvent (from top to bottom). At first sight, the similitude of the SERS and Raman aqueous spectra is not obvious. Such important differences has been also observed by Lai et al. [39]. The significant broadening of the SERS bands, compared to their Raman counterparts can be safely assigned to different orientations of the adsorbed molecules on the metal surface. According to literature data [41, 42], the strong SERS bands observed around 1600 and 1115 cm^{-1} are an indicative of a low concentration (less than 1 $\mu g \cdot ml^{-1}$) of SMX molecules adsorbed on colloidal Ag surfaces.

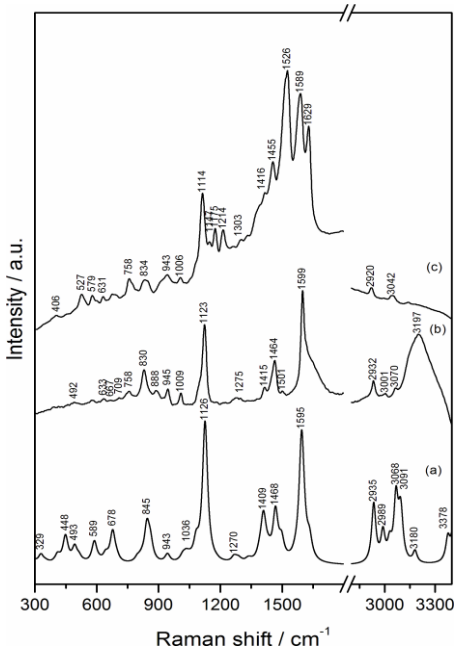

Figure 18. (a) Theoretical Raman spectrum of SMX in aqueous environment solvent, (b) experimental Raman spectrum of SMX in aqueous solution and (c) experimental SERS.

According to the SERS surface-selection rules [35, 36], the normal modes, with a change in the polarizability component perpendicular to the surface are enhanced. Theoretically, the interaction of SMX with the silver surface can be established through the lone electron pairs of the O, N and S atoms, as well as through the π electrons of the two rings.

The Raman spectrum of SMX adsorbed on Ag slab was calculated as an attempt to clarify the adsorption of molecule and the theoretical Raman shifts are included in Table 7.

The SERS spectrum of SMX presents intense bands in the 1500-1630 cm^{-1} region. The band located at 1526 cm^{-1} corresponds to a combination of stretching vibrations in the benzeneamide ring coupled with C-NH_2 stretching and C=N stretching in isoxazole (mode Q18). The calculated Raman shift in water is 1498 cm^{-1}, while for the SMX@Ag slab complex it is predicted blue-shifted at 1545 cm^{-1}, as observed experimentally. The next band, at 1589 cm^{-1} corresponding to Q19 mode is predicted at 1580 cm^{-1} for the complex, its shift to a lower wavenumber with respect to the Raman spectrum of solvated

molecule being reproduced almost quantitatively. The third band (1629 cm^{-1}) appears as a result of NH_2 bending vibrations (Q20 and Q21 modes). Its position, at relatively higher wavenumber than expected for a free NH_2 group, could be influenced either by the interaction with the surface or with the solvent molecules [34]. The band at 1114 cm^{-1} appears of medium intensity in the SERS spectrum of SMX and is assigned to the symmetric stretching of the sulphonyl group in combination with the C-SO_2 stretching, suggesting the close location of this functional group to the silver surface. As seen in Figs. 17-18, this band occurs as a red-shift of more than 30 cm^{-1} of the Raman bands forming the doublet at 1141 and 1155 cm^{-1} of solid state SMX. A similar behavior of these bands has been observed in case of other sulfa drugs [40].

Molecular electrostatic potentials can help to get insights on the adsorption of molecule on silver colloids [70, 71]. The calculated 3D molecular electrostatic potential (MEP) of SMX indicates that the highest electron density is mainly located on the oxygen atoms from the sulphonyl group and from the O and N atoms in the isoxazole ring.

Summing up the Raman-SERS data and considering also the calculated MEP of the molecule, SMX molecule is absorbed in its neutral form, with the sulphonyl group close to, and the isoxazole ring oriented with the edge toward the Ag surface, while the benzeneamide ring is tilted orientated relative to the surface.

These conclusions inferred from the analysis of SERS spectrum are nicely supported by the DFT calculations on the SMX adsorbed on a silver slab used to simulate the Ag(111) surface. The result of the simulation is presented in Fig.19.

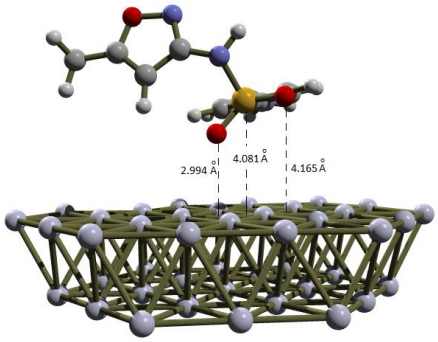

Figure 19. Optimized structure of SMX adsorbed on Ag(111) surface.

The simulation has been done in two steps: (i) first, the SMX molecule has been optimized on periodic slab of Ag(111) composed of 120 silver atoms (see computational details section). The top layer of the slab was relaxed during the optimization. (ii) Then, for subsequent optimization with the B3LYP functional, the slab has been reduced to 42 silver atoms and all the silver atoms were kept fixed.

As seen in Fig.19, the SO_2 group is bound asymmetric to the surface, the shortest distance between the O atom and the top layer of the silver slab is 2.994 Å, while the second O atom of the group is at 4.165 Å. The distances between the centroids of the benzenamide and isoxazole rings and the top layer are 4.175 Å and 6.103 Å, respectively. Moreover, the dihedral angle between the plane defined by the benzenamide ring and the top layer is 13.01°, while the isoxazole ring makes a dihedral angle of 71.45° relative to the silver surface.

The adsorption energy of SMX on Ag(111) surface was estimated based on periodic calculations. It is calculated as $E_{ads}=E_{complex}-E_{slab}-E_{SMX}$ and the calculated value is -17.6 kJ/mol without dispersion correction and -89.1 kJ/mol when dispersion correction is included within the DFT-D3 Grimme's formalism [72]. This result is in line with similar calculations performed on different systems, as reported for instance by Reckien et al. [62] in case of formamide adsorbed on Ag(111) surface.

In summary, the FTIR, FT-Raman, Raman aqueous and SERS spectra of sulfamethoxazole were assigned based on the DFT calculated spectra. Using proper models in calculations, a good correlation between the experimental and theoretical data was obtain, which is a clear evidence for a reliable assignment of the vibrational modes of the studied molecule. With respect to the study of Chamundeeswari et al. [47], six normal modes of the investigated molecule have been reassigned in light of the present theoretical results.

Based on the SERS experimental results and the calculated MEP distribution, the molecule-silver surface interaction was qualitatively derived. It was established that the sulphonyl group is mainly responsible for the interaction with the silver surface. Moreover, the isoxazole ring is directed with the edge toward the silver particles, while the benzeneamide ring have a tilted orientation relative to surface. The experimental data are supported by DFT calculations performed on a complex consisting of SMX molecule adsorbed on an Ag(111) slab.

Table 7 Selected experimental FTIR/ATR, FT-Raman, Raman and SERS bands, together with calculated wavenumbers of SMX

Mode	Experimental wavenumbers (cm^{-1})				Calculated wavenumbers (cm^{-1})				Band assignments
	FTIR/ ATR	Raman	Raman aq.	SERS	IR	Raman	Raman aq	Raman SMX@Ag slab	
Q1	-	501	-	527	-	502	493	534	$\omega(SO_2)+\gamma$(CH,ring1)
Q2	-	545	-	579	-	554	-	585	$\omega(SO_2)+\delta$(CCC,ring1)
Q3	-	631	633	631	-	648	642	644	δ(CCC,ring1)
Q4	682	687	-	-	686	687	678	683	γ(CC,CN,ring2)+γ(CC,ring1) *ν(CS)+δ(CCC,ring1)*
Q5	827 839	829 841	830	834	811 843	811 842	821 845	806 848	ip(ring2)+γ(CH)+ν(NS) *γ(ring1,CH)*
Q6	884	885	888	-	898	898	883	914	ν(SN)+ δ(ring1)+δ(ring2)
Q7	927	925	945	943	921	921	943	-	δ(ring2)+$\rho(CH_3)$
Q8	1014	1011	1009	1006	1022	1023	1018	1008	δ(ring1)
Q9	1027	1026	-	-	1038	1038	1033	1049	δ(ring2)+$\rho(CH_3)$
Q10	1091	1091	1086	1076	1090	1088	1084	1087	$\nu_{sym}(SO_2)+\nu$(C-SO_2)+δ(CCC,ring2)
Q11	1143 1155	1141 1155	1123	1114	1135 1141	1134 1143	1126	1132	$\nu_{sym}(SO_2)+\nu$(C-SO_2)
Q12	1188	1188	-	1175	1187	1187	1181	1181	δ(CH,ring1)+ν(CC,ring1)
Q13	1266	1266	1275	1263	1263	1266	1271	1272	$\nu_{as}(SO_2)+\nu$(CO,ring2)+δ(C19N17H) +$\rho(CH_3)$

Q14	1303	1303	-	1303	1303	1301	1297	1302	ν(C-NH_2 HB)+ν(CC,ring1) *ν(CC,ring1)*
Q15	1313	1313	-	1334	1324	1325	1340	1341	ν(CC,ring1)+ $\nu_{as}(SO_2)$+δ(NH)
Q16	1364 1382	1369 1380	-	-	1388 1400	1387 1401	1409	1442	ν(C=N,ring2)+δ(CH_3)
Q17	1439 1469	1434 1465	1415 1464	1416 1455	1438 1460	1440 1461	1468	1475	ν(CN)+ν(CC,ring2)+δ(CH_3)
Q18	1501	1508	1501	1526	1496 1501	1495 1502	1498	1545	ν(CC,ring1)+ν(C-NH_2)+ν(C=N,ring2)
Q19	1596	1591	1599	1589	1580 1592	1580 1589	1595	1580	ν(CC,ring1)+δ(NH_2) ν(CC,ring2)+ν(C=N,ring2)
Q20	1617	1616	1618	-	1612	1612	-	1614	δ(NH_2)
Q21	-	1636	1641	1629	1629 1639	1629 1639	1630	1614	δ(NH_2 HB)
Q22	-	2930	2932	2920	2931	2931	2935	-	$\nu_{sym}(CH_3)$
Q23	-	3066	3070	-		3055 3082 3090	3068 3091	-	ν(CH,ring1)
Q24	3144	3144	-	-	3194	3184 3194	3180	-	ν(CH) ν(NH)
Q25	3298	3299	-	-	3340	3340	-	-	$\nu_{sym}(NH_2)$ HB
Q26	3377	3379	-	-	3384	3384	3378	-	$\nu_{sym}(NH_2)$ non-HB
Q27	3467	-	-	-	3492	3492	3520	-	$\nu_{asym}(NH_2)$ HB

ν-stretching, δ-bending, ρ-rocking, ω-wagging, γ-out of plane bending, ip.-in plane, ring1: benzene ring, ring2: isoxazole ring, HB-hydrogen bonded. *Italic* is used when the values for the solvated SMX in water differ from those resulted from calculations on SMX trimer.

Characterization and discrimination of Gram - positive bacteria using Raman and SERS spectroscopies

Bacteria constitute a large domain of prokaryotic microorganisms that are present everywhere. Based on their characteristic staining properties under the microscope, where they either do not stain or are decolorized by alcohol during Gram's method of staining, bacteria are classified in Gram – positive and Gram – negative bacteria, thus the main differences between those two types lie in the cell wall components.

A Gram – positive bacterium has a thick, multilayered cell wall consisting mainly of peptidoglycan (up to 80 nm in thickness), also named murein that surrounds the cytoplasmic membrane. The peptidoglycan layer is a porous meshlike exoskeleton that allows diffusion of metabolites to the plasma membrane and is essential for the structure, replication, and survival of the bacteria. This represents 40-80% of the dry weight of the wall [73], teichoic acids and polysaccharides, all these components being commonly surrounded by a paracrystalline surface layer (S-layer) made of proteins [74]. It has relatively few aminoacids, no lipids, but large amounts of sugars and amino sugars [75], such as glucose, rhamnose, glucosamine and muramic acid.

The two bacteria studied in this work are Gram – positive, rod shaped bacterial species of genus *Lactobacillus (Lactobacillus casei ATCC 393)* and *Listeria (Listeria monocytogenes ATCC 19115).*

Lactobacillus casei (L. casei) is a Gram – positive, nonsporing, anaerobic bacterium that has been widely recognized for the attributes and properties beneficial to the human body [76]. It is a harmless, nonpathogenic microorganism that protects the human body from disease by producing lactic acid, which helps lower pH levels in the digestive system and impedes the growth of harmful bacteria. The World Health Organization and the Food and Agriculture Organization of the United Nations categorized *L. casei* as probiotics.

Listeria monocytogenes (L. monocytogenes) is one of the most virulent food-borne pathogenic bacterium with an extended shelf life, and also the cause of listeriosis.

In the last years, a continuing growing interest was shown towards the development of new routine detection methods for microorganism identification, that are less time - consuming and more sensitive than the available ones. Among the new

procedures, molecular methods like vibrational spectroscopy techniques gain a lot of attention and popularity in clinical, but also in food applications. Advantages, like the accuracy of the obtained results, the minimal sample preparation, and ability to probe samples under *in-vivo* conditions without the necessity of markers [77] made the IR and Raman spectroscopy reliable alternatives for identification and discrimination of bacteria at the strain level. A particular interest was shown towards SERS, due to several advantages over Raman technique, like the possibility of single-molecule detection and small concentration of the sample to be analyzed. Due to the particular fingerprint of each bacterium, the vibrational methods can be used independently or in combination with multivariate analysis for detection and characterization.

The aim of the study was to apply Raman and SERS spectroscopic techniques for identification and characterization of two Gram-positive bacteria species, namely *L. casei ATCC 393* and *L. monocytogenes ATCC 19115*. Firstly, the experimental parameters were optimized in order to obtain reproducible and high resolution spectra. Secondly, by combining the spectroscopic methods with Principal Component Analysis (PCA), the possibility of bacterial species discrimination was tested.

Experimental section

Bacteria cultivation. *L. casei ATCC 393* was purchased in lyophilized form (Microbiologics, Minnesota, USA) and grown in de Man, Rogosa, Sharpe (MRS) broth (Oxoid, UK). Routinely, the inoculum cultures were obtained from freeze-dried cells suspended in 5 mL MRS, incubated under aerobic conditions at 37 ^{o}C (24 h) and then sub-cultured into 95 mL MRS and incubated in the same conditions [78]. The inoculum cultures were grown for 24 h in a 200-mL Erlenmeyer flask containing 100 mL MRS, mixed on a rotary shaker (Heidolph Unimax 1100, Germany) at 37 ^{o}C. *L. monocytogenes ATCC 19115* was maintained on Oxford agar (Sifin, Germany) plates at 4°C. A single colony of *L. monocytogenes* was inoculated into a tube of tryptic soy broth plus 0.7% yeast extract (TSBYE) (Difco Laboratories) and incubated at 35 °C for 24 h.

The cell growth was monitored by UV-spectrometry (Nanodrop ND-1000 Spectrophotometer, Nanodrop Technologies, USA) by measuring the media optical density at 600 nm. In case of *L. casei*, the sample concentration was found to be 10^{14}

CFU/ml (O.D. = 0.95), while the sample concentration of *L. monocytogenes* was determined to be 10^{11} CFU/ml (O.D. = 0.7.

Colloid synthesis. The silver nanoparticles (AgNPs) were synthesized using the procedure proposed by Leopold and Lendl [26].

Instrumentation. AFM imaging was performed using a commercial NT-MDT NTEGRA Spectra (Russia) microscope, at room temperature. Images were taken in dynamic intermittent-contact mode with a silicon cantilever (NSG30-A, NT-MDT) whose nominal spring constant was 40 N/m and a tip radius of < 10 nm. After acquisition, image treatment was performed using Nova v1.1.0.1837 (NT-MDT) SPM software.

The Raman and SERS spectra of the bacteria were obtained on a conventional Renishaw inVia Raman Microscope equipped with a HeNe laser (632.8 nm) with a total laser power of 50 mW. In order to avoid the sample photodegradation, neutral density filters were used for laser power reduction, the following experiments taking place at laser powers in 0.05 – 2.5 mW interval. The instrument was wavelength calibrated using a silicon wafer focused under the 50× objective and collected as a static spectrum centered at 521 cm^{-1} for 1 s.

Experimental details. For Raman and SERS measurements, 2 ml of bacteria culture were centrifuged (6000 rpm, 10 min) and the culture medium was removed. The cell pellet was washed 3 times with 2 ml of MilliQ water (18 $M\Omega \cdot cm^{-1}$ resistivity) and centrifuged in the same previous conditions. The harvested pellet of *L. casei* was resuspended in 1 mL MilliQ water and the harvested pellet of *L. monocytogenes* was resuspended in 250 µl MilliQ water for all the measurements. The SERS suspensions were prepared by mixing 500 µl of *a priori* prepared colloid with 5 µl bacteria. The *in situ* SERS samples were prepared as described by Zhou et al. [79].

All the spectroscopic experiments were carried out by drying 5 µl of washed bacteria / SERS suspension onto MgF_2 disks and focused under the 50× objective. Each Raman spectrum is the result of 10 accumulations of 10 s integration time each. In case of the SERS spectra, each one is a result of 3 accumulations of 5 s per each accumulation.

The WiRE software package was used for instrument control and data capture. The Raman spectra were collected as extended scan in the wavenumber range of 400 - 1800 cm^{-1}, while all the SERS spectra were collected as static spectra in the wavenumber range

of 600 - 1700 cm^{-1}. For background reduction, 5 spectra for each sample were collected in the same experimental conditions, and the average spectrum is depicted. The next step was the normalization to the peak with the highest intensity. Particularly, for the SERS spectra a baseline correction in 10 points and a FFT smoothing correction in 5 points for background reduction were applied.

Chemometric analysis. PCA is a multivariate technique used to analyze the inherent structure of the data, by reducing the dimensionality of the data set and finding an alternative set of coordinates, the principal components (PCs) [77, 80, 81]. By plotting the PC-loadings as a function of the variables, it reveals the regions related to the differences founded in the data set. In this study, PCA was performed over the Raman and SERS spectra of *L. casei* and *L. monocytogenes*, with the aim of discriminating, based on the inherent structure of the spectral data, the two bacterial species. PCA was carried out using the software Unscrambler X 10.0 (CAMO Software, Norway) on the unprocessed data.

Results and discussion

The viability of the washed samples was evaluated using AFM technique, and the aquired images are illustrated in Figs. 20 and 21.

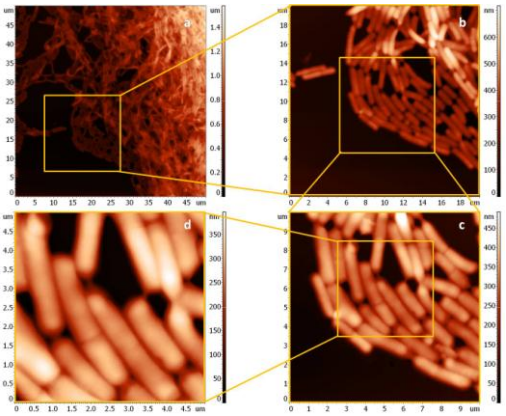

Figure 20. AFM images of *L. casei*. **(a)** 50 µm × 50 µm; **(b)** 20 µm × 20 µm; **(c)** 10 µm × 10 µm and **(d)** 5 µm × 5 µm.

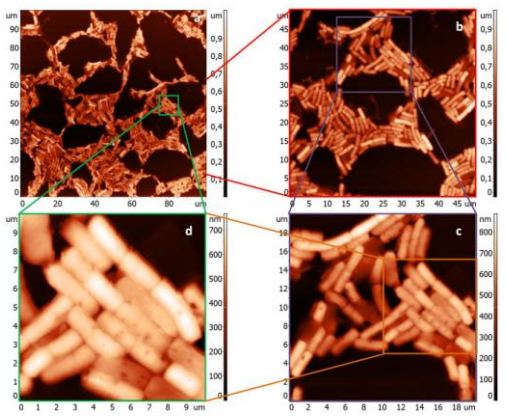

Figure 21. AFM images of *L. monocytogenes*. **(a)** 100 µm × 100 µm; **(b)** 50 µm × 50 µm; **(c)** 20 µm × 20 µm and **(d)** 10 µm × 10 µm.

Raman spectra of *L. casei* and *L. monocytogenes*

The information gain from typical Raman spectra of microorganisms is related to cell wall composition and cytoplasmic components. The little concentration of phosphorus in the *L. casei* cell wall was an indication for the lack of teichoic acids [75]. The anionic character of the *L. casei* cell envelope is given by the lipoteichoic acid (LTA) [74], made in this case of poly(glycerophosphate) substituted with D-alanyl ester residues [82]. Although the S-layer is a common wall component for *L. casei* species, the study of Vadillo-Rodriguez et al. [83] showed that *L. casei ATCC 393* doesn't possess a S-layer, but instead is rich in polysaccharides [84]. The cell wall of *L. monocytogenes* has the typical structure of Gram-positive bacteria. The Raman spectra of *L. casei* and *L. monocytogenes* are presented in Figure 22 and strongly resemble to each other.

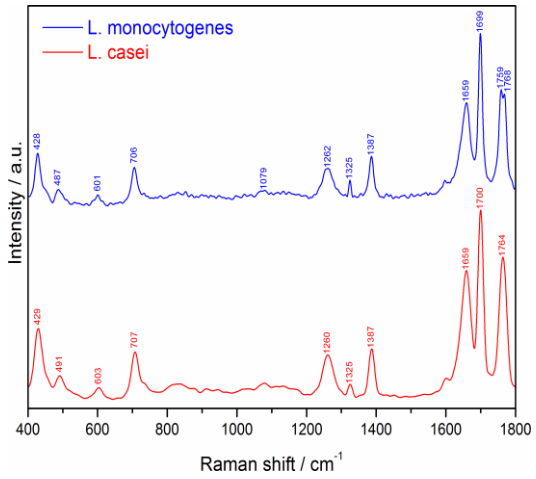

Figure 22. Raman spectra of *L. monocytogenes* (top) and *L. casei* (bottom).

The peaks located in the region 1690 cm^{-1} - 1770 cm^{-1} are tipically assigned to C=O ester stretching group, as proposed by Maquelin et al. [85] and Lu et al. [86]. The amide I band from the unsaturated lipids usually appears around 1650 cm^{-1} [77, 87, 88] and in our Raman spectra is located at 1659 cm^{-1}, while amide III band is at 1260 cm^{-1} (1262 cm^{-1} for *L. monocytogenes*), as also seen by Gaus et al. [87] and Mobili et al. [89]. The adenine vibrations give rise to the bands present at 707 cm^{-1} (706 cm^{-1} in the *L. monocytogenes* spectrum), 1325 and 1387 cm^{-1}, respectively. The last two bands are also the result of guanine, tyrosine and uracil nucleobases vibrations in case of the 1325 cm^{-1} band, and of thymine vibrations in case of the 1387 cm^{-1} band. These last two bands were assigned based on the results reported by Gaus et al. [87]. All the molecules that give Raman bands in the spectra of the studied bacteria are components of the typical Gram – positive bacteria [73]. Due to the slight or no differences between the Raman spectra of the two species, statistical methods of data analysis are needed for the discrimination of the two species. Furthermore, Raman spectra contain abundant chemical

and structural information that can be exploited by applying a multivariate analysis over the attained results.

SERS spectra of *L. casei* and *L. monocytogenes*

The SERS results of *L. casei* and *L. monocytogenes* obtained with *a priori* prepared colloid and the ones obtained by using *in situ* synthesized AgNPs are illustrated in Figs. 23 and 24.

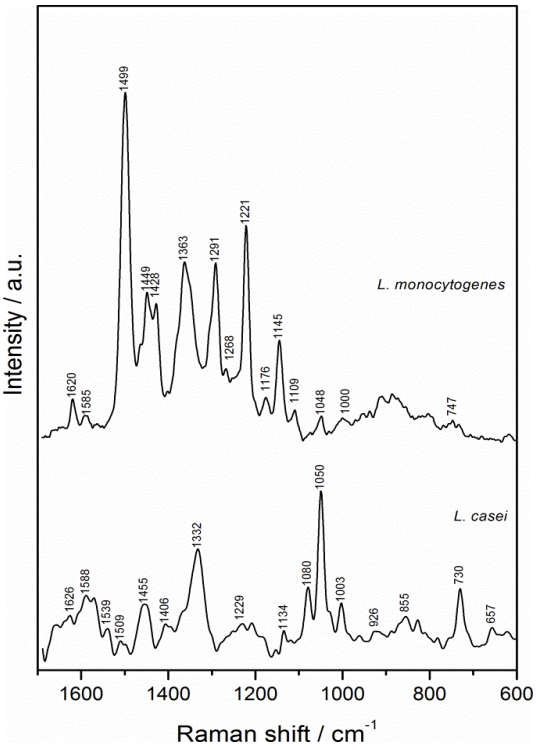

Figure 23. SERS spectra using *a priori* prepared Ag colloid of *L. monocytogenes* (top) and *L. casei* (bottom).

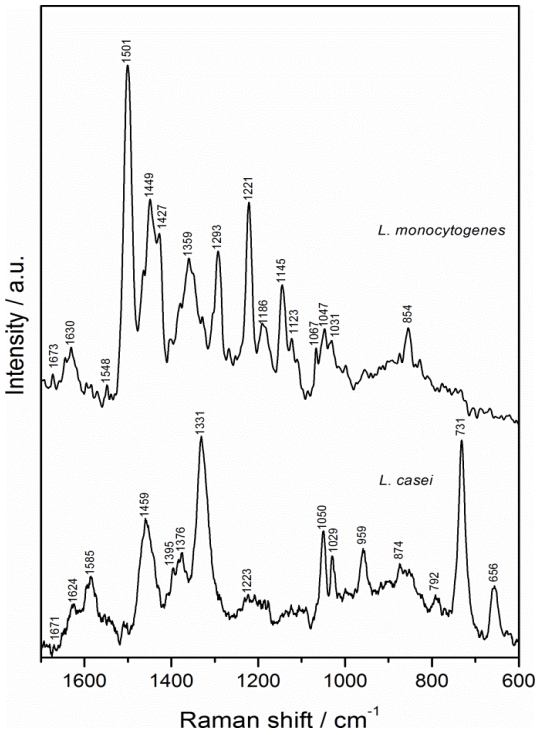

Figure 24. SERS spectra using *in situ* synthesized Ag nanoparticles of *L. monocytogenes* (top) and *L. casei* (bottom).

The spectra can be analyzed from different perspectives: (i) the observation of spectral differences due to the use of two different methods for SERS detection; (ii) the comparison of the spectral fingerprint of the two species, and finally, (iii) to find the similarities or the differences between our results and previous reported results of Mircescu et al. [90] in terms of viability of *in situ* synthesis of AgNPs and its use in detection or discrimination of various strains and species of microorganisms. All the recorded spectra present several common bands, independently of the type of AgNPs synthesis method. In case of *L. casei*, both SERS spectra show bands located around 657

cm^{-1}, 730 cm^{-1}, 1050 cm^{-1}, 1332 cm^{-1}, 1455 cm^{-1}, 1588 cm^{-1} and at 1626 cm^{-1}, with very little variations in their position. This fact happens also in the case of the SERS spectra of *L. monocytogenes*.

These bands are mostly well defined in both spectral pictures, and present very small variations in their positions and intensity. The reason of the differences could be related to the scattering effects that are commonly met in SERS experiments, as also reported by Mircescu et al. [90], but also in the absorption sites of AgNPs. Major intensity differences can be observed in the SERS spectra of *L. casei*. These bands are typically DNA nucleobases vibrations, particularly assigned to adenine (the bands at 730, 1050, 1332/1331 cm^{-1}) [90-94] or CH_2 deformations of saturated lipids (the band at 1455/1459 cm^{-1}) [90, 91]. This last band was also observed by Prucek et al. [95] at 1456 cm^{-1} in the SERS spectra of other Gram-positive bacteria species and was assigned to COH vibrations of oligosaccharides. One explanation could be related to the smaller possibility of *a priori* prepared AgNPs to reach inside the cell in comparison to the *in situ* synthesized AgNPs. It is worth mentioning that the 1050 cm^{-1} band was also assigned by some authors to C-O stretching of glucose [96], as the cell wall structure of *L. casei* is made of large amounts of sugars and amino sugars. In case of the SERS spectra of *L. monocytogenes*, the band intensities are comparable. Interestingly, the SERS bands mainly correspond to cell wall vibrations components: the band at 1145 cm^{-1} is the results of CC, CO, COH deformations in carbohydrates [97] or C-C stretching in lipids [93], the band at 1221 cm^{-1} is assigned to amide III [98], while the band at 1291/1293 cm^{-1} represents CH deformations in proteins [98]. The next band, at 1363/1359 cm^{-1} is ascribed to CH deformations of proteins or $\nu(COO^-)$ symmetric deformations [93, 99] and the 1428/1427 cm^{-1} and 1449 cm^{-1} bands are CH_2 deformations of saturated lipids [91]. Only one band, situated at 1620/1630 cm^{-1} is attributed to DNA nucleobases interaction with AgNPs [91]. In conclusion, in case of *L. monocytogenes*, the AgNPs interact mainly with the cell wall components, while in the case of *L. casei* the AgNPs interact with the genetic code, inside the cell.

On the other hand, our *in situ* SERS results show several resemblances, but also some discrepancies, in comparison with the SERS spectra obtained by Mircescu et al. [90]. The resemblances lie in the presence of DNA nucleobase vibrations in the same regions of the SERS spectra, and may be explained based on the close similarities of the internal components of Positive- and Negative-bacteria. The SERS spectra of *E. coli*

shows multiple bands associated to the phospholipid bilayer outside of the peptidoglycan layer, as this membrane is thought to be in close proximity to the SERS substrate. Our spectra are generally composed of peaks arising from the AgNPs interaction with the peptidoglycan layer, the lipoteichoic acids or the glucose, as the cell wall of *L. casei* was demonstrated to be made of ≈ 43 % glucose [75].

Principal component analysis of *L. casei* and *L. monocytogenes*

The spectral differences between the two Gram-positive bacteria species were evaluated in the PC space by using PCA method. Ten Raman spectra of *L. casei* and 23 Raman spectra of *L. monocytogenes* within 420 – 1788 cm^{-1} spectral range were used for the PCA discrimination. In case of the *a priori* SERS spectra, the PCA was applied on 148 SERS spectra of *L. casei* and 62 SERS spectra of *L. monocytogenes* within 600 – 1700 cm^{-1} spectral range. Finally, a number of 83 SERS spectra of *L. casei* and 11 SERS spectra of *L. monocytogenes*, within the same spectral range as previously SERS spectra, but obtained using *in situ* synthesized AgNPs, were used for PCA discrimination. The entire data was preprocessed using the Multiplicative Scatter Correction (MSC) and the first derivative, with 10 points smoothing.

- **PCA results on the Raman spectra**

Figure 25 depicts the PCA scores plot of PC-2 *vs* PC-1 obtained for the Raman analysis of *L. casei* and *L. monocytogenes*. The two Gram-positive bacteria are exemplary separated along the PC-1 axis, which explains the 23 % of the total variance in the data set.

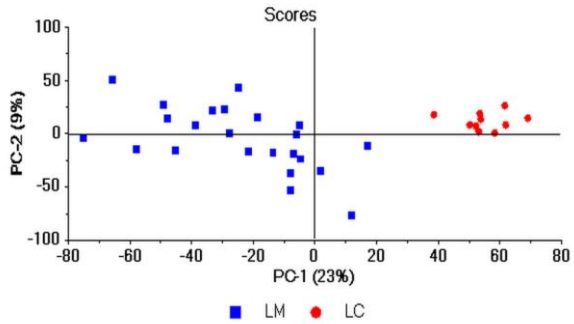

Figure 25. PCA score of Raman spectra showing the separation of *L. monocytogenes* and *L. casei*.

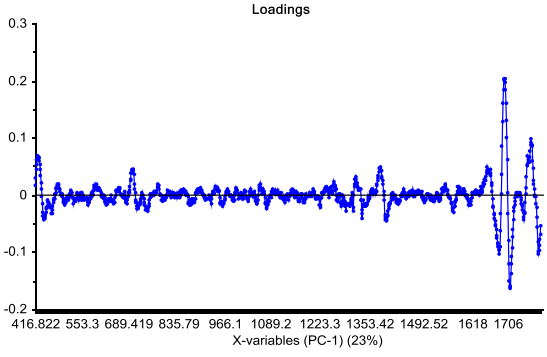

Figure 26. PC-loadings corresponding to the PCA result shown in Figure 25.

The PC-1 loadings values are plotted in Fig. 26 and represent the regions of the Raman spectra where the differences among the bacterial species are more evident. The differentiation mainly takes place in the 1600-1800 cm^{-1} region, but also in the 1300 – 1400 cm^{-1}. The highest contribution in discriminating *L. casei* and *L. monocytogenes* samples is correlated with the Raman band located at 1700 cm^{-1}. Other significant contributions come from the bands that appear in the Raman spectra at 1759 cm^{-1} and at 1768 cm^{-1}, respectively.

- **PCA results on the *a priori* SERS spectra**

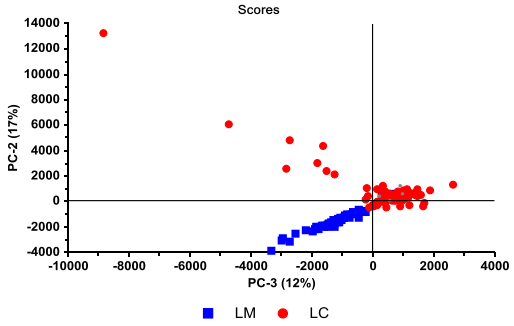

Figure 27. PCA score of SERS spectra obtained using *a priori* prepared Ag colloid for *L. monocytogenes* and *L. casei* separation.

The PCA scores plot of PC-2 *vs* PC-3 (Fig. 27) conducted over the *a priori* SERS spectra show a clear separation between *L. casei* and *L. monocytogenes* after PC-3 and after PC-2, which explains 12 % and 17 %, respectively of the total variance of the data set. According to PC-3 and PC-2 (Fig. 28 **(a)** and **(b)**) loadings plots, the differences appear in 700-750 cm^{-1} and 1200-1400 cm^{-1} regions and at ≈1490 cm^{-1}.

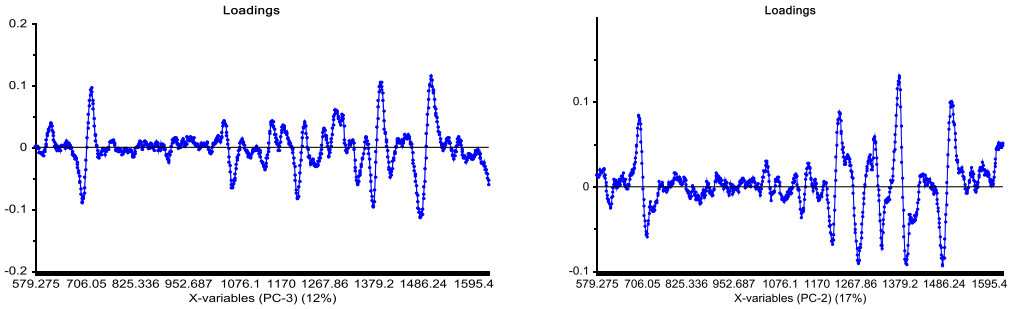

(a) **(b)**

Figure 28. PC-loadings corresponding to the PCA result shown in Figure 27.

- **PCA results on the *in situ* SERS spectra**

The PCA scores plot of PC-4 *vs* PC-3 conducted over the *in situ* SERS spectra is presented in Fig. 29.

The separation between *L. casei* and *L. monocytogenes* is made along PC-4 and PC-3 axis and explains 1 % and 5 %, respectively of the total variance of the data set (Fig. 30 **(a)** and **(b)**). According to the PC-loadings plots (Fig. 30 **(a)** and **(b)**), the spectral diferences that contribute to the discrimination between the species are related to the 731 cm^{-1} SERS band and the SERS bands located in the 1145 – 1500 cm^{-1} region.

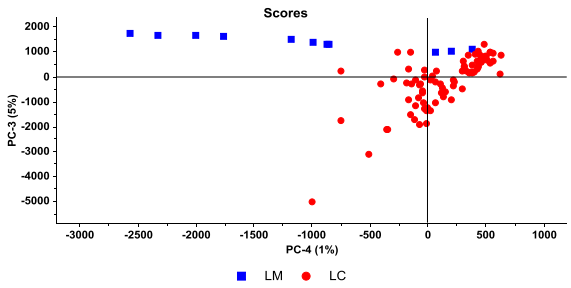

Figure 29. PCA score of SERS spectra obtained using *in situ* prepared Ag colloid for *L. monocytogenes* and *L. casei* separation.

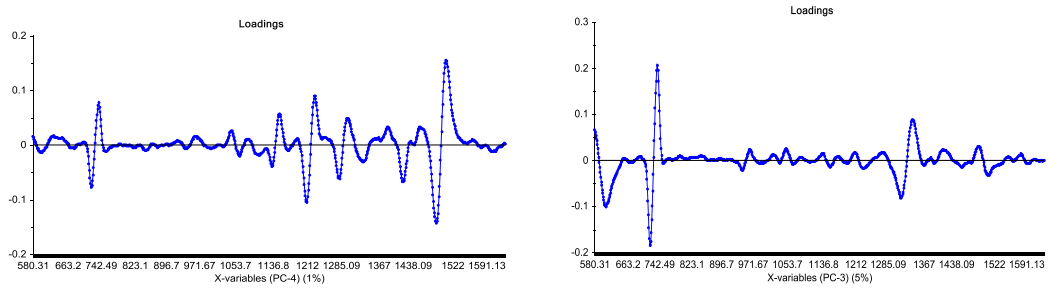

(a) **(b)**

Figure 30. PC-loadings corresponding to the PCA result shown in Figure 29.

In conclusion, two Gram-positive bacteria species were successfully characterized and discriminated using Raman and SERS spectroscopic methods, in combination with PCA unsupervised method. The Raman spectra of *L. casei* and *L. monocytogenes* are very similar in the bands position and their intensity. The spectra are composed of bands arising mainly from the DNA nucleobases, but also from the unsaturated lipids from the peptidoglycan layer. The existing differences between *L. casei* and *L. monocytogenes* were observed only after applying PCA on the experimental results and their discrimination was successfully made.

In case of the SERS analysis, two methods for SERS detection were used. All the SERS spectra contain several common bands, independently of the AgNPs synthesis method. Major intensity differences were observed in the SERS spectra of *L. casei.* These bands arise from DNA nucleobases vibrations or saturated lipids vibrations. The SERS

spectra of *L. monocytogenes* are very similar and composed of bands arising from the cell wall components, thus sugesting the interaction of AgNPs mainly with the peptidoglycan layer and the lipid components. Also in the case of the SERS spectra, PCA analysis was applied and demonstrated the possibility of discrimination between the two Gram-positive bacteria based on the SERS experimental spectra.

GENERAL CONCLUSIONS

The aim of this thesis was to optimize the physico-chemical parameters of nanometer gold thin films, and of some biomolecular systems with possible applications in the quality life improvement.

In the first experimental chapter are reported the results obtained in the process of parameters optimization in case of thin Au films with flat atomic terraces on Si(111) substrate, deposited using molecular beam epitaxy technique. The effects of substrate temperature and deposition rate on the orientation and surface morphology of the Au thin films were evaluated using scanning tunneling microscopy and X-ray diffraction methods. The results suggest that the best compromise between roughness and grain size was found to occur for a substrate temperature maintained at 580 $^{\circ}$C and a deposition rate of 1.6 nm/min.

The second part was focused on the structural investigation of two common antibiotics by means of vibrational spectroscopic methods (FTIR/ATR, FT-Raman and surface-enhanced Raman scattering), as well as density functional theory calculations. In case of trimethoprim, a reliable assignment of vibrational IR, Raman and SERS bands was possible by a proper choice of model used in quantum chemical calculations. Based on the SERS spectrum analysis it was shown that the molecule is adsorbed on the silver surface through the pyrimidine ring, in a perpendicular orientation. Two theoretical models were used in order to simulate the silver surface and the interaction with trimethoprim molecule, the accuracy of the models being evaluated by comparing the predicted bands position of the two complexes with the SERS result.

The above mention methods were also employed for the characterization of the sulfamethoxazole molecule. Particular emphasis was put on the adsorption geometry of the molecule to the silver colloidal nanoparticles surface. FTIR/ATR, FT-Raman, Raman aqueous solution and SERS spectra of SMX were assigned based on DFT calculations with the hybrid B3LYP exchange-correlation functional, coupled with the standard 6-31G(d) basis set. Calculations performed on the SMX molecule adsorbed on a slab constructed to model the Ag(111) surface give quantitative results related to the geometry of the molecule in the vicinity of the silver surface.

The last part of the thesis present the application of Raman and SERS spectroscopic techniques, in combination with PCA multivariate method for Gram-positive bacteria characterization and discrimination. The Raman spectra of *L. casei* and *L. monocytogenes* are very similar in the bands position and their intensity. The spectra are composed of bands arising mainly from the DNA nucleobases, but also from the unsaturated lipids from the peptidoglycan layer. The existing differences between *L. casei* and *L. monocytogenes* were observed only after applying PCA on the experimental results and their discrimination was successfully made.

In case of the SERS analysis, two methods for SERS detection were used. All the SERS spectra contain several common bands, independently of the AgNPs synthesis method. Major intensity differences were observed in the SERS spectra of *L. casei*. These bands arise from DNA nucleobases vibrations or saturated lipids vibrations. The SERS spectra of *L. monocytogenes* are very similar and composed of bands arising from the cell wall components, thus sugesting the interaction of AgNPs mainly with the peptidoglycan layer and the lipid components. Also in the case of the SERS spectra, PCA analysis was applied and demonstrated the possibility of discrimination between the two Gram-positive bacteria based on the SERS experimental spectra.

References

[1] S.W. Han, H.W. Lee, H.J. Lee, J.Y. Kim, J.H. Kim, C.S. Oh, S.H. Choa, Curr. Appl. Phys. 6, Supplement 1 (2006) e81.
[2] G. Kalyuzhny, M.A. Schneeweiss, A. Shanzer, A. Vaskevich, I. Rubinstein, J. Am. Chem. Soc. 123 (2001) 3177.
[3] W.M. Bullis, Solid-State Electron. 9 (1966) 143.
[4] B.A. Movchan, A.V. Demchishin, Fiz. Met. Metalloved. 28 (1969) 653.
[5] J.A. Thornton, Annu. Rev. Mater. Sci. 7 (1977) 239.
[6] C.R.M. Grovenor, H.T.G. Hentzell, D.A. Smith, Acta Metall. Mater. 32 (1984) 773.
[7] R. Messier, A.P. Giri, R.A. Roy, J. Vac. Sci. Technol. A 2 (1984) 500.
[8] P.B. Barna, M. Adamik, Thin Solid Films 317 (1998) 27.
[9] M. Higo, K. Fujita, Y. Tanaka, M. Mitsushio, T. Yoshidome, Appl. Surf. Sci. 252 (2006) 5083.
[10] B.D. Cullity, Elements of X-Ray Diffraction, 2nd ed., Addison-Wesley Publishing Company Inc., USA, 1978.
[11] G.K. Williamson, R.E. Smallman, Philos. Mag. 1 (1956) 34.
[12] P.K.R. Kalita, B.K. Sarma, H.L. Das, Bull. Mater. Sci. 23 (2000) 313.
[13] U. Höpfner, H. Hehl, L. Brehmer, Appl. Surf. Sci. 152 (1999) 259.
[14] E. Holland-Moritz, J. Gordon, G. Borges, R. Sonnenfeld, Langmuir 7 (1991) 301.
[15] H. Klein, W. Blanc, R. Pierrisnard, C. Fauquet, P. Dumas, Eur. Phys. J. B 14 (2000) 371.
[16] S.H. Leuba, J. Zlatanova, Biology at the Single Molecule Level, 1st Edition, in, Pergamon, New York, 2001.
[17] B. Lüssem, S. Karthäuser, H. Haselier, R. Waser, Appl. Surf. Sci. 249 (2005) 197.
[18] D. Marconi, **A. Ungurean**, Appl. Surf. Sci. 288 (2014) 166.
[19] S. Hasegawa, Y. Nagai, T. Oonishi, S. Ino, Phys. Rev. B 47 (1993) 9903.
[20] F. Ruffino, M.G. Grimaldi, J. Appl. Phys. 107 (2010) 104321.
[21] F. Ruffino, V. Torrisi, G. Marletta, M. Grimaldi, Nanoscale Res. Lett. 6 (2011) 112.
[22] A. Taleb-Ibrahimi, C.A. Sebenne, F. Proix, J. Vac. Sci. Technol. A 4 (1986) 2331.
[23] E. Heikkila, O.V. Renkonen, R. Sunila, P. Uurasmaa, P. Huovinen, J. Antimicrob. Chemother. 25 (1990) 275.
[24] J. Sallai, A. Vernyik, G. Regdon, S. Gombkoto, J. Nemeth, G. Regdon, Jr., J. Pharm. Pharmacol. 49 (1997) 496.
[25] **A. Ungurean**, N. Leopold, L. David, V. Chiş, Spectrochim. Acta Part A Mol. Biomol. Spectrosc. 102 (2013) 52.
[26] N. Leopold, B. Lendl, J. Phys. Chem. B 107 (2003) 5723.
[27] M.J. Frisch, G.W. Trucks, H.B. Schlegel, G.E. Scuseria, M.A. Robb, J.R. Cheeseman, G. Scalmani, V. Barone, B. Mennucci, G.A. Petersson, H. Nakatsuji, M. Caricato, X. Li, H.P. Hratchian, A.F. Izmaylov, J. Bloino, G. Zheng, J.L. Sonnenberg, M. Hada, M. Ehara, K. Toyota, R. Fukuda, J. Hasegawa, M. Ishida, T. Nakajima, Y. Honda, O. Kitao, H. Nakai, T. Vreven, J.A. Montgomery, J.E. Peralta, F. Ogliaro, M. Bearpark, J.J. Heyd, E. Brothers, K.N. Kudin, V.N. Staroverov, R. Kobayashi, J. Normand, K. Raghavachari, A. Rendell, J.C. Burant, S.S. Iyengar, J. Tomasi, M. Cossi, N. Rega, J.M. Millam, M. Klene, J.E. Knox, J.B. Cross, V. Bakken, C. Adamo, J. Jaramillo, R. Gomperts, R.E. Stratmann, O. Yazyev, A.J. Austin, R. Cammi, C. Pomelli, J.W. Ochterski, R.L. Martin, K. Morokuma, V.G. Zakrzewski, G.A. Voth, P. Salvador, J.J. Dannenberg, S. Dapprich, A.D. Daniels, Farkas, J.B. Foresman, J.V. Ortiz, J. Cioslowski, D.J. Fox, Gaussian 09, Revision B.01, in, Wallingford CT, 2009.
[28] C. Lee, W. Yang, R.G. Parr, Phys. Rev. B 37 (1988) 785.
[29] A.D. Becke, J. Chem. Phys. 98 (1993) 5648.
[30] A. Kaczor, K. Malek, M. Baranska, J. Phys. Chem. C 114 (2010) 3909.
[31] S. Williams, T. Johnson, T. Gibbons, C. Kitchens, Theor. Chem. Acc. 117 (2007) 283.
[32] A.P. Scott, L. Radom, J. Phys. Chem. 100 (1996) 16502.
[33] GaussView 5.0, Gaussian Inc., in.

[34] G. Socrates, Infrared Characteristic Group Frequencies, 2nd ed., John Wiley: New York, NY, 1994.
[35] J.A. Creighton, Surf. Sci. 124 (1983) 209.
[36] M. Moskovits, J.S. Suh, J. Phys. Chem. 88 (1984) 5526.
[37] Zhao, L. Jensen, G.C. Schatz, J. Am. Chem. Soc. 128 (2006) 2911.
[38] J.M. Mullin, J. Autschbach, G.C. Schatz, Comp. Theor. Chem. 987 (2012) 32.
[39] K. Lai, F. Zhai, Y. Zhang, X. Wang, B. Rasco, Y. Huang, Sens. & Instrumen. Food Qual. 5 (2011) 91.
[40] W.S. Sutherland, J.J. Laserna, M.J. Angebranndt, J.D. Winefordner, Anal. Chem. 62 (1990) 689.
[41] R. Montes, J.J. Laserna, Analyst 115 (1990) 1601.
[42] C.G. Blatchford, J.R. Campbell, J.A. Creighton, Surf. Sci. 120 (1982) 435.
[43] A.A. Muthu Prabhu, G. Venkatesh, N. Rajendiran, J. Solution Chem. 39 (2010) 1061.
[44] T. Arslan, F. Kandemirli, E.E. Ebenso, I. Love, H. Alemu, Corros. Sci. 51 (2009) 35.
[45] C. Topacli, A. Topacli, J. Mol. Struct. 644 (2003) 145.
[46] B. Kesimli, A. Topacli, C. Topacli, J. Mol. Struct. 645 (2003) 199.
[47] S.P. Vijaya Chamundeeswari, E. James Jebaseelan Samuel, N. Sundaraganesan, Spectrochim. Acta, Part A 118 (2014) 1.
[48] **A. Ungurean,** M. Oltean, L. David, N. Leopold, J.P. Prates Ramalho, V. Chiş, J. Mol. Struct. 1073 (2014) 71.
[49] Sigma-Aldrich, Product Information: Sulfamethoxazole, in.
[50] P.C. Lee, D. Meisel, J. Phys. Chem. 86 (1982) 3391.
[51] M. Cyrankiewicz, T. Wybranowski, S. Kruszewski, J. Phys. Conf. Ser. 79 (2007) 012013.
[52] S.E.J. Bell, N.M.S. Sirimuthu, J. Phys. Chem. A 109 (2005) 7405.
[53] J. Tomasi, B. Mennucci, R. Cammi, Chem. Rev. 105 (2005) 2999.
[54] P. Borowski, J. Phys. Chem. A 116 (2012) 3866.
[55] G. Kresse, J. Hafner, Phys. Rev. B 47 (1993) 558.
[56] G. Kresse, J. Furthmüller, Phys. Rev. B 54 (1996) 11169.
[57] G. Kresse, J. Furthmüller, Comp. Mater. Sci. 6 (1996) 15.
[58] J.P. Perdew, K. Burke, M. Ernzerhof, Phys. Rev. Lett. 77 (1996) 3865.
[59] P.E. Blöchl, Phys. Rev. B 50 (1994) 17953.
[60] G. Kresse, D. Joubert, Phys. Rev. B 59 (1999) 1758.
[61] M. Ge, B. Zhong, W.G. Klemperer, A.A. Gewirth, J. Am. Chem. Soc. 118 (1996) 5812.
[62] W. Reckien, B. Kirchner, F. Janetzko, T. Bredow, J. Phys. Chem. C 113 (2009) 10541.
[63] L.A. LaJohn, P.A. Christiansen, R.B. Ross, T. Atashroo, W.C. Ermler, J. Chem. Phys. 87 (1987) 2812.
[64] W. Zhou, D.E. Moore, J. Photochem. Photobiol. B Biol. 39 (1997) 63.
[65] A.L. Boreen, W.A. Arnold, K. McNeill, Environ. Sci. Technol. 38 (2004) 3933.
[66] A.C.D. Inc., ACD/pKa DB, version 12.0, in, Toronto, ON, Canada, 2012.
[67] C.P. Price, A.L. Grzesiak, A.J. Matzger, J. Am. Chem. Soc. 127 (2005) 5512.
[68] L. Maury, J. Rambaud, B. Pauvert, Y. Lasserre, G. Berge, M. Audran, Can. J. Chem. 63 (1985) 3012.
[69] M. Takasuka, H. Nakai, Vib. Spectrosc. 25 (2001) 197.
[70] P. Politzer, D.G. Truhlar, Chemical Applications of Atomic and Molecular Electrostatic Potentials, Plenum, New York, 1981.
[71] D. Beveridge, R. Lavery, Theoretical Biochemistry & Molecular Biophysics, Volume 2, Adenine Press, Schenectady, New York, 1991.
[72] S. Grimme, J. Antony, S. Ehrlich, H. Krieg, J. Chem. Phys. 132 (2010).
[73] W. Jiang, A. Saxena, B. Song, B.B. Ward, T.J. Beveridge, S.C. Myneni, Langmuir 20 (2004) 11433.
[74] J. Delcour, T. Ferain, M. Deghorain, E. Palumbo, P. Hols, A. van Leeuw. J. Microb. 76 (1999) 159.
[75] M. Ikawa, E.E. Snell, J. Biol. Chem. 235 (1960) 1376.

[76] W.H. Holzapfel, P. Haberer, R. Geisen, J. Bjorkroth, U. Schillinger, Am. J. Clin. Nutr. 73 (2001) 365S.
[77] P. Mobili, A. Londero, G. De Antoni, A. Gomez-Zavaglia, Rev. Mex. Fis. 56 (2010) 378.
[78] D. Vodnar, C. Socaciu, Chem. Cent. J. 6 (2012) 61.
[79] H. Zhou, D. Yang, N.P. Ivleva, N.E. Mircescu, R. Niessner, C. Haisch, Anal. Chem. 86 (2014) 1525.
[80] H. Martens, T. Naes, Multivariate Calibration Wiley, Chichester, England, 1989.
[81] C.H. Esbensen, Multivariate Data Analysis - in practice, 5th ed., CAMO Process AS, Esbjerg, Denmark, 2005.
[82] W.C. Childs, 3rd, D.J. Taron, F.C. Neuhaus, J. Bacteriol. 162 (1985) 1191.
[83] V. Vadillo-Rodriguez, H.J. Busscher, W. Norde, J. de Vries, H.C. van der Mei, J. Bacteriol. 186 (2004) 6647.
[84] H.C. van der Mei, J. de Vries, H.J. Busscher, Surf. Sci. Rep. 39 (2000) 1.
[85] K. Maquelin, C. Kirschner, L.P. Choo-Smith, N. van den Braak, H.P. Endtz, D. Naumann, G.J. Puppels, J. Microbiol. Methods 51 (2002) 255.
[86] X. Lu, H. Al-Qadiri, M. Lin, B. Rasco, Food Bioprocess. Technol. 4 (2011) 919.
[87] K. Gaus, P. Rosch, R. Petry, K.D. Peschke, O. Ronneberger, H. Burkhardt, K. Baumann, J. Popp, Biopolymers 82 (2006) 286.
[88] C. Fan, Z. Hu, A. Mustapha, M. Lin, Appl. Microbiol. Biotechnol. 92 (2011) 1053.
[89] P. Mobili, C. Araujo-Andrade, A. Londero, C. Frausto-Reyes, R.I. Tzonchev, G.L. De Antoni, A. Gomez-Zavaglia, J. Dairy Res. 78 (2011) 233.
[90] N.E. Mircescu, H. Zhou, N. Leopold, V. Chis, N.P. Ivleva, R. Niessner, A. Wieser, C. Haisch, Anal. Bioanal. Chem. 406 (2014) 3051.
[91] A. Walter, A. Marz, W. Schumacher, P. Rosch, J. Popp, Lab Chip 11 (2011) 1013.
[92] M. Kahraman, K. Keseroglu, M. Culha, Appl. Spectrosc. 65 (2011) 500.
[93] N.P. Ivleva, M. Wagner, A. Szkola, H. Horn, R. Niessner, C. Haisch, J. Phys. Chem. B 114 (2010) 10184.
[94] L. Zeiri, B.V. Bronk, Y. Shabtai, J. Eichler, S. Efrima, Appl. Spectrosc. 58 (2004) 33.
[95] R. Prucek, V. Ranc, L. Kvitek, A. Panacek, R. Zboril, M. Kolar, Analyst 137 (2012) 2866.
[96] S. Sivakesava, J. Irudayaraj, D. Ali, Process Biochem. 37 (2001) 371.
[97] K.C. Schuster, I. Reese, E. Urlaub, J.R. Gapes, B. Lendl, Anal. Chem. 72 (2000) 5529.
[98] M. Kahraman, M.M. Yazıcı, F. Şahin, M. Çulha, Langmuir 24 (2008) 894.
[99] A. Sengupta, M.L. Laucks, N. Dildine, E. Drapala, E.J. Davis, J. Aerosol Sci. 36 (2005) 651.

List of publications

Papers published in ISI Journals

- **A. Ungurean,** N. Leopold, L. David, V. Chiș, **Vibrational spectroscopic and DFT study of trimethoprim,** Spectrochimica Acta Part A: Molecular and Biomolecular Spectroscopy 102 (2013) 52–58.
- **A. Ungurean**, M. Oltean, L. David, N. Leopold, J. P. Prates Ramalho, V. Chiș, **Adsorption of sulfamethoxazole molecule on silver colloids: A joint SERS and DFT study,** Journal of Molecular Structure 1073 (2014) 71-76.
- D. Marconi, **A. Ungurean, The effect of substrate temperature on structural and morphological properties of Au/Si(1 1 1) thin films,** Applied Surface Science 288 (2014) 166-171.
- A. I. G. Petrehele, D. Rusu, **A. Ungurean,** G. L. Turdean, E. Indrea, L. David, M. Rusu, **Structural and physico-chemical study of new Keggin polyoxometalates with mixed addenda**, Chemistry Magazine 65 (2014) 265-271.

Papers published in non ISI Journals

- D. Rusu, D. Mare, C. Berindean, **A. Ungurean**, O. Baban, L. David, **Spectroscopic studies of lacunary polyoxotungstates Cerium (III) complexes based on α-B-$[Bi^{III}W_9O_{33}]^{9-}$ units,** Studia UBB Physica 57(LVII) 1 (2012) 87 - 92.

Submitted papers

- **A. Colniță**, D. Marconi, I. Turcu, **Fabrication of interdigitated electrodes using molecular beam epitaxy and optical lithography**, Analytical Letters, 2014.
- D. Marconi, **A. Colniță**, I. Turcu, **The influence of deposition rate on structural and morphological properties of Au/Si(111) growth using molecular beam epitaxy method**, Analytical Letters, 2014.

Manuscript in preparation

- **A. Ungurean-Colniță**, N. E. Dina, N. Leopold, D. C. Vodnar, V. Chiș, L. David, **Characterization and discrimination of Gram - positive bacteria using Raman spectroscopy,** 2014.

Oral and poster presentations

International conferences

- **A. Ungurean**, N. Leopold, S. Schlücker, S. Niebling, V. Chiș, L. David, **SERS experimental and DFT study of Trimethoprim,** 14th European Conference on the Spectroscopy of Biological Molecules **(ECSBM 2011),** 29th Aug. - 3rd Sept. 2011**,** Coimbra, Portugal (**Poster**).
- **A. Ungurean**, N. Leopold, S. Schlücker, S. Niebling, V. Chiș, L. David, **A theoretical study of the SERS spectrum of Trimethoprim adsorbed on silver clusters**, 4th Conference on Advanced Spectroscopies on Biomedical and Nanostructured Systems **(BioNanoSpec 2011)**, 4-7th September 2011, Cluj-Napoca, Romania **(Poster)**.
- **A. Ungurean**, N. Leopold, V. Chiș, L. David, **Theoretic and vibrational spectroscopy investigations of Trimethoprim**, International Conference on Sciences, 11-12th November 2011, Oradea, Romania (**Oral presentation**).
- **A. Ungurean**, M. Oltean, L. David, N. Leopold, V. Chiș, **A spectroscopic study of Sulfamethoxazole adsorbed on silver nanoparticles**, 31st European Congress of Molecular Spectroscopy **(EUCMOS 2012)**, 26th -31st August 2012, Cluj-Napoca, Romania **(Poster)**.
- D. Rusu, A. I. G. Petrehele, **A. Ungurean**, M. Hubner, G. Borodi, M. Rusu, L. David, **Structural and physical - chemical study of the new Keggin polyoxometalates with mixed addenda**, 31st European Congress of Molecular Spectroscopy **(EUCMOS 2012)**, 26th -31st August 2012, Cluj-Napoca, Romania **(Poster)**.
- D. Marconi, **A. Ungurean**, R. Bratfalean, **The influence of deposition rate on structural and morphological properties of gold thin films on Si (111),** 9th International Conference on Processes in Isotopes and Molecules **(PIM 2013),** 25-27th September 2013, Cluj-Napoca, Romania **(Poster)**.
- **A. Colniță**, D. Marconi, I. Turcu, **Fabrication of interdigitated electrodes using molecular beam epitaxy and optical lithography techniques and its applications in molecular detection**, The 3rd International Conference on Analytical and Nanoanalytical Methods for Biomedical and Environmental Sciences **(IC-ANMBES 2014)**, 13-15th June 2014, Brasov, Romania (**Oral presentation**).
- D. Marconi, **A. Colniță**, I. Turcu, The effect of substrate temperature on structural and morphological properties of Au/Si(111) thin films, The 3rd International Conference on Analytical and Nanoanalytical Methods for Biomedical and Environmental Sciences **(IC-ANMBES 2014)**, 13-15th June 2014, Brasov, Romania **(Awarded Poster).**
- **A. Colniță,** N.E. Dina, D. Vodnar, N. Leopold, V. Chiș, L. David**, Characterization of gram positive bacteria using Raman spectroscopy,** The 3rd

International Conference on Analytical and Nanoanalytical Methods for Biomedical and Environmental Sciences **(IC-ANMBES 2014)**, 13-15th June 2014, Brasov, Romania **(Poster).**

- **A. Colniță**, N. E. Dina, D. Vodnar, N. Leopold, V. Chiș, L. David, **The use of Raman spectroscopy in Gram-positive bacteria detection and characterization,** 5th Conference on Advanced Spectroscopies on Biomedical and Nanostructured Systems (**BioNanoSpec 2014**) 7-10th September 2014, Cluj-Napoca, Romania **(Poster)**.

National conferences

- **A. Ungurean**, N.E. Mircescu, N. Leopold, D. Vodnar, L. David, **Label-free bacteria detection using Raman spectroscopy**, 12th National Conference on Biophysics **(NCB 2013)** – Biophysics for Health, with International Participation, 13-16th June 2013, Iaşi, Romania **(Poster)**.

Other scientific activities

- Participation to the International Course **"Electroporation for Medicine: Basic Knowledge, Applications and Technologies"**, organized by Carol Davila Medical University and Romanian Society of Pure and Applied Biophysics within the frame and with the financial support of the COST Action TD 1104, 25 – 27th October 2012, Bucharest, Romania.
- Participation to the Satellite Workshop "**Current reports on synthetic peptides, metals and molecular adaptors interaction with protein pores and reconstituted lipid membrane systems",** organized in the frame of **IC-ANMBES 2014,** 11-12th June 2014, Brasov, Romania. **Oral presentation** with the title "**Nanoimprint lithography: A versatile tool for high resolution nanofabrication".**